THE UNIVERSITY of EDINBURGH

Edinburgh Research Explorer

Plastin and spectrin cooperate to stabilize the actomyosin cortex during cytokinesis

Citation for published version:
Sobral, AF, Chan, FY, Norman, MJ, Osório, DS, Dias, AB, Ferreira, V, Barbosa, DJ, Cheerambathur, D, Gassmann, R, Belmonte, JM & Carvalho, AX 2021, 'Plastin and spectrin cooperate to stabilize the actomyosin cortex during cytokinesis', *Current Biology*, vol. 31, no. 24, pp. 5415-5428.e10. https://doi.org/10.1016/j.cub.2021.09.055

Digital Object Identifier (DOI):
10.1016/j.cub.2021.09.055

Link:
Link to publication record in Edinburgh Research Explorer

Document Version:
Publisher's PDF, also known as Version of record

Published In:
Current Biology

General rights
Copyright for the publications made accessible via the Edinburgh Research Explorer is retained by the author(s) and / or other copyright owners and it is a condition of accessing these publications that users recognise and abide by the legal requirements associated with these rights.

Take down policy
The University of Edinburgh has made every reasonable effort to ensure that Edinburgh Research Explorer content complies with UK legislation. If you believe that the public display of this file breaches copyright please contact openaccess@ed.ac.uk providing details, and we will remove access to the work immediately and investigate your claim.

OPEN ACCESS

Download date: 08. Jun. 2022

Article

Current Biology

Plastin and spectrin cooperate to stabilize the actomyosin cortex during cytokinesis

Graphical abstract

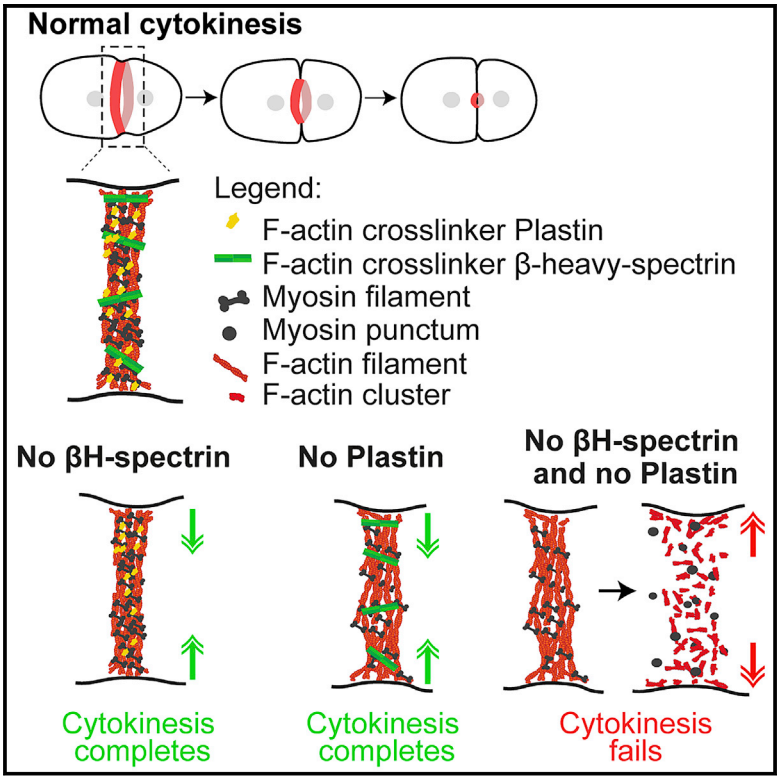

Authors

Ana Filipa Sobral, Fung-Yi Chan, Michael J. Norman, ..., Reto Gassmann, Julio Monti Belmonte, Ana Xavier Carvalho

Correspondence

anacarvalho@ibmc.up.pt

In brief

Sobral, Chan et al. address how F-actin crosslinkers contribute to cytokinesis. Cooperation between the small/rigid crosslinker plastin and the large/flexible crosslinker βH-spectrin is shown to be essential for organization and stability of the equatorial actomyosin network that forms the cytokinetic ring.

Highlights

- Single inhibitions of F-actin crosslinkers do not lead to cytokinesis failure
- Cytokinesis fails upon double inhibition of the crosslinkers plastin and βH-spectrin
- Their joint loss collapses the actomyosin network that forms the cytokinetic ring
- Ring assembly with these two distinct crosslinker types is modeled *in silico*

Sobral et al., 2021, Current Biology *31*, 5415–5428
December 20, 2021 © 2021 The Authors. Published by Elsevier Inc.
https://doi.org/10.1016/j.cub.2021.09.055

CellPress

Current Biology

CellPress
OPEN ACCESS

Article

Plastin and spectrin cooperate to stabilize the actomyosin cortex during cytokinesis

Ana Filipa Sobral,[1,2,3,7] Fung-Yi Chan,[1,2,7] Michael J. Norman,[4,5] Daniel S. Osório,[1,2] Ana Beatriz Dias,[1,2] Vanessa Ferreira,[1,2] Daniel J. Barbosa,[1,2] Dhanya Cheerambathur,[6] Reto Gassmann,[1,2] Julio Monti Belmonte,[4,5] and Ana Xavier Carvalho[1,2,8,*]

[1]Instituto de Investigação e Inovação em Saúde (i3S), Universidade do Porto, 4200-135 Porto, Portugal
[2]IBMC - Instituto de Biologia Molecular e Celular, Universidade do Porto, 4200-135 Porto, Portugal
[3]ICBAS - Instituto de Ciências Biomédicas Abel Salazar, Universidade do Porto, 4050-313 Porto, Portugal
[4]Department of Physics, North Carolina State University, Raleigh, NC 27695, USA
[5]Quantitative and Computational Developmental Biology Cluster, North Carolina State University, Raleigh, NC 27695, USA
[6]Wellcome Centre for Cell Biology, University of Edinburgh, Edinburgh EH9 3BF, UK
[7]These authors contributed equally
[8]Lead contact
*Correspondence: anacarvalho@ibmc.up.pt
https://doi.org/10.1016/j.cub.2021.09.055

SUMMARY

Cytokinesis, the process that partitions the mother cell into two daughter cells, requires the assembly and constriction of an equatorial actomyosin network. Different types of non-motor F-actin crosslinkers localize to the network, but their functional contribution remains poorly understood. Here, we describe a synergy between the small rigid crosslinker plastin and the large flexible crosslinker spectrin in the *C. elegans* one-cell embryo. In contrast to single inhibitions, co-inhibition of plastin and the βH-spectrin (SMA-1) results in cytokinesis failure due to progressive disorganization and eventual collapse of the equatorial actomyosin network. Cortical localization dynamics of non-muscle myosin II in co-inhibited embryos mimic those observed after drug-induced F-actin depolymerization, suggesting that the combined action of plastin and spectrin stabilizes F-actin in the contractile ring. An *in silico* model predicts that spectrin is more efficient than plastin at stabilizing the ring and that ring formation is relatively insensitive to βH-spectrin length, which is confirmed *in vivo* with a *sma-1* mutant that lacks 11 of its 29 spectrin repeats. Our findings provide the first evidence that spectrin contributes to cytokinesis and highlight the importance of crosslinker interplay for actomyosin network integrity.

INTRODUCTION

The actin cytoskeleton is necessary for a wide range of cellular processes that require force generation and cell-shape changes, including cell division, cell motility, and tissue morphogenesis.[1] Generation and propagation of contractile force requires myosin II motors and non-motor crosslinkers (crosslinkers hereafter). Bipolar myosin II filaments slide actin filaments past one another at the expense of ATP, while crosslinkers maintain F-actin network connectivity during filament sliding.[1]

Depending on their size, structural flexibility, and concentration, crosslinkers bridge F-actin into networks of different complexities and mechanical properties.[2] Smaller crosslinkers, such as α-actinin and plastin, tend to form tight parallel actin bundles, while larger crosslinkers, such as filamin and spectrins, organize F-actin into loosely crosslinked meshworks.[3–6] Crosslinkers may additionally differ in their subcellular localization and response to tension and may have other functions apart from F-actin crosslinking. How F-actin networks organize and behave in the presence of multiple crosslinkers remains poorly explored.

During cytokinesis, animal cells assemble a contractile ring at the cell equator beneath the plasma membrane, and subsequent ring constriction ultimately leads to separation of the two daughter cells.[7] The contractile ring consists of formin-nucleated non-branched F-actin that aligns circumferentially in a tight band. Besides non-muscle myosin II (hereafter myosin), other ring components include crosslinkers such as α-actinin, fimbrin/plastin (hereafter plastin), anillin, and septins.[7] While myosin has long been known to be essential for cytokinesis,[7] the role of crosslinkers remains unclear. When depleted individually, only cortexillins in *D. discoideum* and anillin in *D. melanogaster* and mammalian cultured cells have been shown to cause significant cytokinesis failure.[8–10] However, cortexillins are not well conserved between species, and anillin is a multifunctional protein that interacts with several contractile ring components,[10] so its other functions also contribute to cytokinesis. The only known example of functional redundancy among crosslinkers during cytokinesis is between fission yeast α-actinin and fimbrin.[11]

In the present study, we describe a synergy between plastin and spectrin, two crosslinkers that are highly conserved through evolution. Plastin and spectrin belong to the calponin homology (CH) domain superfamily of crosslinkers (like filamin, α-actinin, and dystrophin), whose actin-binding domains consist of a double calponin-like sequence.

This is an open access article under the CC BY-NC-ND license (http://creativecommons.org/licenses/by-nc-nd/4.0/).

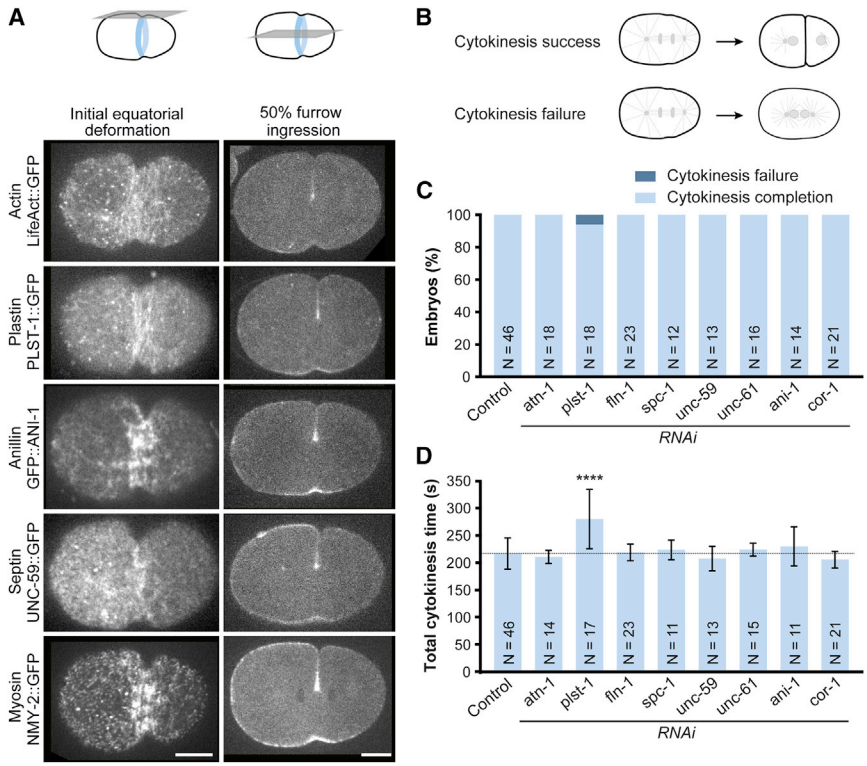

Figure 1. Cytokinesis completes when F-actin crosslinkers are depleted individually

(A) Images of the cortex (left) and central plane (right) in *C. elegans* one-cell embryos expressing fluorescent markers of actin, plastin, anillin, septins, and myosin at initial equatorial deformation and 50% furrow ingression, respectively. Scale bars, 10 μm.

(B) Schematic illustrating cytokinesis completion or failure during the first embryonic division.

(C) Percentage of one-cell embryos that complete/fail cytokinesis after RNAi-mediated depletion of crosslinkers. N indicates the number of embryos analyzed.

(D) Total cytokinesis time (mean ± 95% CI), defined as the interval between anaphase onset and the contractile ring reaching a diameter of 5 μm (see STAR Methods for details), in embryos depleted of crosslinkers. N indicates the number of embryos analyzed. Statistical significance was determined using one-way ANOVA followed by Dunnett's multiple comparison test: ****$p \leq 0.0001$.

See also Figure S1 and Tables S1 and S2.

Plastin is a small globular protein composed of two EF hands and two adjacent actin-binding domains (ABDs). Plastin binds branched and non-branched F-actin and assembles F-actin into tightly packed bundles in parallel or antiparallel orientation *in vitro*.[6,12,13] Plastin has been described to localize in cytokinetic rings, neurons, intestinal microvilli, hair cell stereocilia, and fibroblast filopodia, and to contribute to cytokinesis, invasion by pathogenic bacteria, endocytosis, and epidermal morphogenesis.[13–16]

Spectrins are large and flexible crosslinkers that have not been previously implicated in cytokinesis. The functional form of spectrin consists of two antiparallel heterodimers of β-spectrin and α-spectrin.[17] The resulting tetramers are elongated rods with ABDs at either end. Spectrins also contain a pleckstrin homology (PH) domain and interact with plasma membrane-bound proteins, thus linking the actomyosin cytoskeleton to the plasma membrane.[17] There are two types of β-spectrin, referred to as conventional β-spectrin and heavy β-spectrin (βH), which differ in the number of spectrin repeats and subcellular localization.[17,18] Tetramers of conventional β-spectrin protect the cortex from mechanical stresses in erythrocytes and axons, where they form regular polygonal or longitudinal F-actin networks, respectively.[5,19] They are also required for ciliogenesis and the ability to sense and respond to external mechanical stimuli in *C. elegans*.[20,21] βH-spectrin was shown to have mechanosensitive properties and to accumulate in regions of higher tension in *D. melanogaster* muscle cells.[22] Furthermore, βH-spectrin is involved in embryonic development and tissue morphogenesis in *D. melanogaster* and *C. elegans*.[23,24]

C. elegans contains one ortholog each for plastin (*plst-1*), α-spectrin (*spc-1*), conventional β-spectrin (*unc-70*), and βH-spectrin (*sma-1*).[13,23,25,26] This contrasts with vertebrates, which express three plastins, two α-spectrins, four β-spectrins, and one βH-spectrin in a tissue-specific manner.[14,17,18] The fact that these and other crosslinkers are represented by a single gene in *C. elegans* facilitates functional studies aimed at uncovering synergies among crosslinkers. Here, we find that, in contrast to single inhibitions, co-inhibition of plastin and βH-spectrin results in penetrant cytokinesis failure in the *C. elegans* one-cell embryo. Combining engineered βH-spectrin mutants with analysis of myosin and F-actin dynamics, we demonstrate that plastin and βH/α-spectrin jointly organize and stabilize cortical F-actin at the cell equator, which is critical for contractile ring assembly. Our results emphasize the importance of understanding how different types of crosslinkers cooperate to organize actomyosin networks *in vivo*.

RESULTS

Multiple crosslinkers localize to the equatorial cell cortex and the tip of the ingressing cleavage furrow during cytokinesis

To assess localization dynamics of crosslinkers in one-cell *C. elegans* embryos undergoing their first cytokinesis, we used fluorescent versions of plastin (PLST-1::GFP), anillin (GFP::ANI-1), and septin (UNC-59::GFP) (Table S1). Cortical imaging allowed visualization of contractile ring assembly at the cell equator, and central plane imaging during furrow ingression offered a side view of the constricting contractile ring (Figure 1A). PLST-1::GFP formed linear bundles at the equatorial cortex and a meshwork with distinct puncta in the surrounding cortex. This localization pattern was similar to that of F-actin (LifeAct::GFP), as reported previously.[13] By contrast, GFP::ANI-1 and UNC-59::GFP localized to cortical patches that were enriched in the

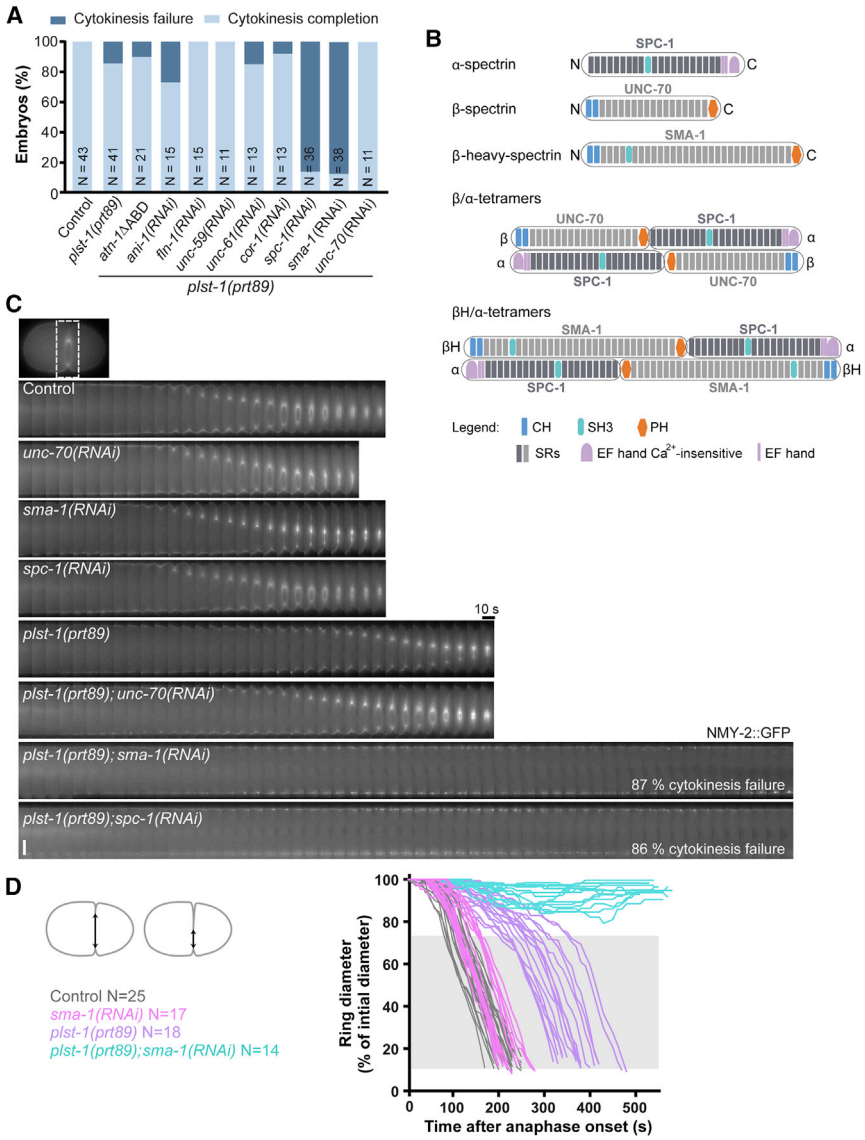

Figure 2. Inhibiting PLST-1 together with SPC-1 or SMA-1, but not UNC-70, results in cytokinesis failure

(A) Percentage of cytokinesis completion/failure in one-cell embryos after crosslinker co-inhibition.

(B) Schematic illustrating the two types of spectrin tetramers: α-spectrin (SPC-1) pairs with either conventional β-spectrin (UNC-70) or βH-spectrin (SMA-1). CH, calponin homology domain; SH3, Src homology domain; PH, pleckstrin homology domain; SR, spectrin repeat.

(C) Representative kymographs of the equatorial region in one-cell embryos. The first frame corresponds to anaphase onset. Scale bar, 10 μm.

(D) Individual curves of contractile ring diameter over time after anaphase onset. Gray zone indicates the region corresponding to 75%–10% furrow ingression, which was used to calculate ring constriction rate. N indicates the number of embryos analyzed.

See also Video S1 and Tables S1 and S2.

equatorial region, similar to myosin (NMY-2::GFP). UNC-59::GFP was more prominent on the anterior cortex than GFP::ANI-1 and NMY-2::GFP. All probes were strongly enriched at the tip of the ingressing furrow during contractile ring constriction. These results illustrate that cytokinesis occurs in the presence of multiple crosslinkers, consistent with the idea that different types of crosslinkers jointly organize the actomyosin network.

A survey of nine conserved crosslinkers identifies plastin/PLST-1 as the only crosslinker whose depletion slows cytokinesis

To analyze crosslinker function during cytokinesis, we first identified *C. elegans* crosslinker orthologs that are highly conserved across species and have been demonstrated to crosslink F-actin *in vitro*:[9,27–32] α-actinin (*atn-1*), plastin (*plst-1*), filamin (*fln-1*), β-spectrin (*unc-70*), βH-spectrin (*sma-1*), septins (*unc-59* and *unc-61*), anillin (*ani-1*), and coronin (*cor-1*). Cytokinesis completed successfully and with normal timing when ATN-1, FLN-1, SPC-1, UNC-59, UNC-61, ANI-1, and COR-1 were individually depleted by RNAi (Figures 1B–1D; note that *spc-1(RNAi)* also inhibits UNC-70 and SMA-1, the other spectrin complex subunits). Depletion of each crosslinker was validated as described in Figure S1. Depletion of PLST-1 slowed cytokinesis (278 ± 54 s versus 217 ± 29 s in controls), and 6% of *plst-1(RNAi)* embryos failed to complete furrowing (Figures 1C and 1D). Ring constriction rate (the slope of the linear region between ~75% and 10% furrow ingression) was not affected after *plst-1(RNAi)* (0.19 ± 0.04 μm/s versus 0.19 ± 0.02 μm/s in controls), confirming that PLST-1 acts primarily at the early stages of cytokinesis (ring assembly and furrow initiation) (Figure 2D).[13,16] We conclude that among the nine conserved crosslinkers examined, only PLST-1 depletion impacts cytokinesis in the *C. elegans* one-cell embryo.

Co-inhibition of PLST-1 and βH-spectrin/SMA-1 results in cytokinesis failure

To address potential cooperation between PLST-1 and other crosslinkers during cytokinesis, we combined the *plst-1(prt89)* mutant, which carries a premature stop in its open reading frame,[16] with RNAi-mediated depletion of ANI-1, FLN-1, UNC-59, UNC-61, COR-1, or SPC-1 (Figure 2A). Additionally, we combined *plst-1(prt89)* with an *atn-1* mutant that lacks the actin-binding domain (*atn-1ΔABD*). We found that *spc-1(RNAi)* in *plst-1(prt89)* embryos was the only condition that significantly increased cytokinesis failure (86% failure in *plst-1(prt89);spc-1(RNAi)* versus 15% in *plst-1(prt89)*; Figures 2A and 2C; Video S1). Since the α-spectrin SPC-1 can form tetramers with either the conventional β-spectrin UNC-70 or the βH-spectrin SMA-1 (Figure 2B), we next performed *unc-70(RNAi)* or *sma-1(RNAi)* in *plst-1(prt89)* embryos. Similar to

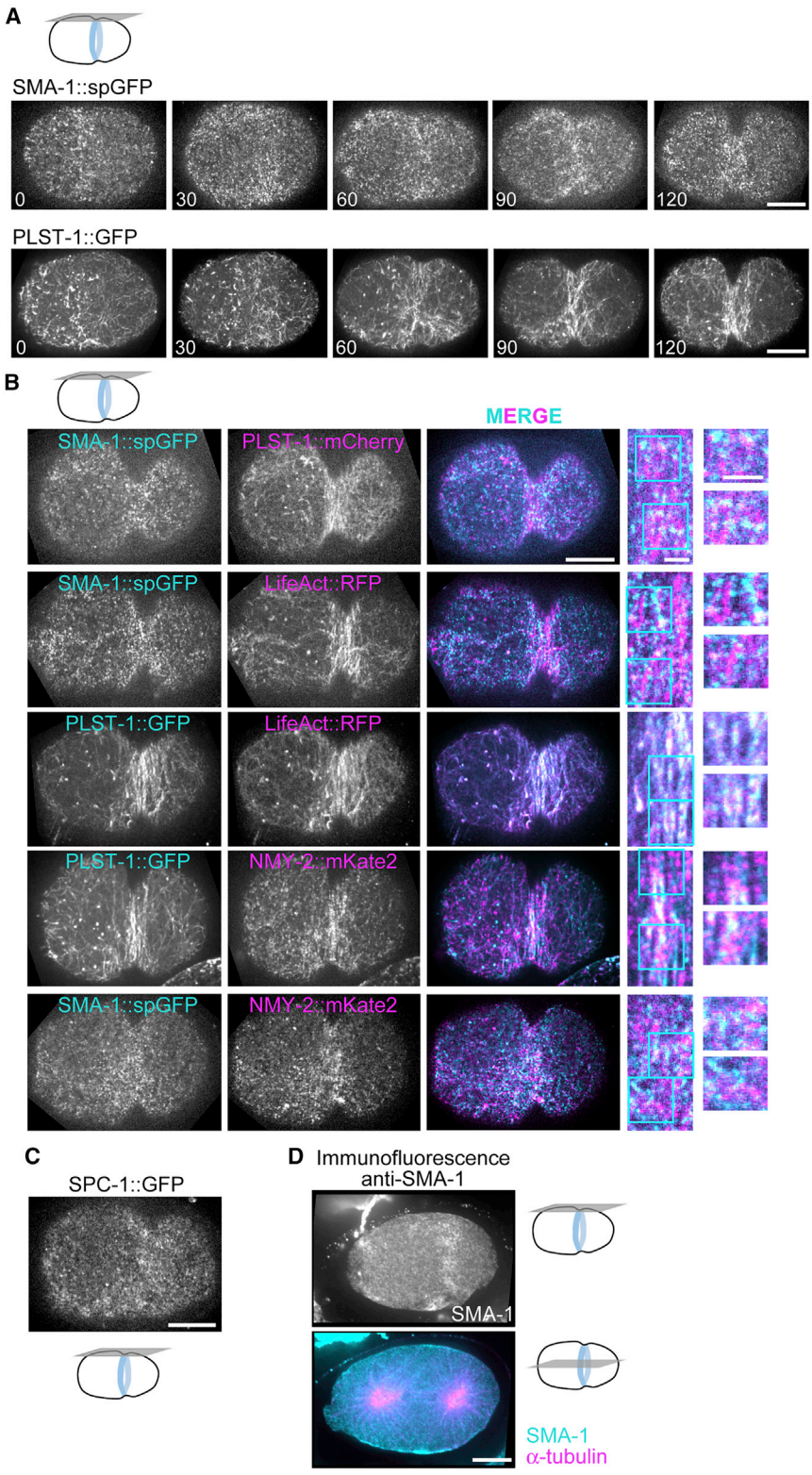

Figure 3. PLST-1 and SMA-1 show distinct profiles of localization on the cell cortex

(A) Images of the cortex in one-cell embryos expressing SMA-1::spGFP (splitGFP) or PLST-1::GFP. Numbers indicate the time in seconds after anaphase onset. Scale bars, 10 μm.

(B) Images of the cortex in one-cell embryos co-expressing either the two fluorescent crosslinkers or one of the fluorescent crosslinkers and fluorescent LifeAct or NMY-2. Scale bar, 10 μm. Blow-ups of the equatorial region are shown on the right. Scale bars, 2 μm.

(C) Image of the cortex in a one-cell embryo expressing SPC-1::GFP. Scale bar, 10 μm.

(D) Images of the cortex and central plane of a fixed one-cell embryo stained with anti-SMA-1 and anti-α-tubulin antibodies. Scale bars, 10 μm.

See also Figure S7A and Tables S1 and S2.

plst-1(prt89);spc-1(RNAi), *plst-1(prt89);sma-1(RNAi)* caused cytokinesis failure in 87% of embryos, which were unable to form a cytokinetic furrow (Figures 2A–2D; Video S1). Consistent with the RNAi results, we were unable to generate viable double mutants carrying *plst-1(prt89)* and the null mutant *sma-1(ru18)*.[23] Homozygous *sma-1(ru18);plst-1(prt89)* animals that reached adulthood laid on average 2 embryos. 95% of the laid progeny died during embryogenesis and 5% arrested at the L1 stage. In contrast to *sma-1(RNAi);plst-1(prt89)*, *unc-70(RNAi);plst-1(prt89)* had no further adverse effects on cytokinesis beyond those observed in *plst-1(prt89)* alone (Figures 2A and 2C), which is in agreement with the minimal expression of UNC-70 in the early embryo.[21,26] We conclude that SPC-1/SMA-1 α/βH-spectrin tetramers become essential for cytokinesis in the absence of PLST-1.

PLST-1 and SMA-1 have distinct localization profiles at the cell cortex

To assess SMA-1 localization during cytokinesis, we generated a fluorescent version using the split GFP(spGFP) approach, in which the 11-stranded β-barrel structure of GFP is reconstituted from two separately expressed fragments: GFP1-10 (β strands 1–10) and GFP11 (β strand 11).[33] We inserted 6 tandem copies of GFP11 downstream of the *sma-1* open reading frame by genome editing and crossed animals expressing endogenous SMA-1::6xGFP11 with animals expressing transgenic GFP1-10 under the control of a germline promoter. Imaging of one-cell embryos revealed that the SMA-1::spGFP signal was significantly dimmer than that of PLST-1::GFP and formed small cortical dots that became enriched at the cell equator simultaneously with PLST-1::GFP (Figures 3A and S7A). While

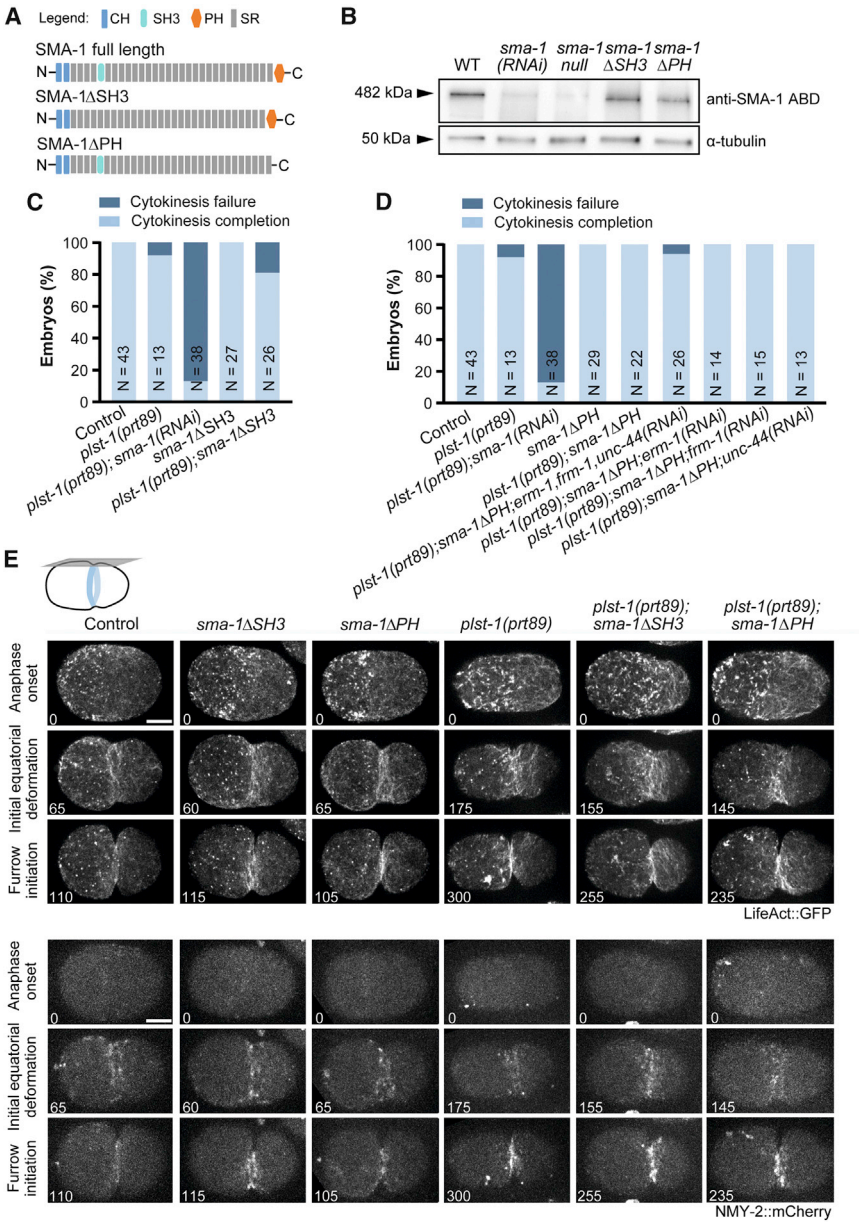

Figure 4. Synergy between SMA-1 and PLST-1 does not require SMA-1-mediated F-actin network anchoring to the plasma membrane or SMA-1 SH3 domain-mediated signaling

(A) Schematic of wild-type SMA-1, SMA-1ΔSH3, and SMA-1ΔPH. CH, calponin homology domain; SH3, Src homology domain; PH, pleckstrin homology domain; SR, spectrin repeat.

(B) Immunoblots of adult lysate with an affinity-purified antibody raised against the actin-binding domain (ABD) of SMA-1. α-tubulin serves as the loading control.

(C and D) Percentage of cytokinesis completion/failure in one-cell embryos. N indicates the number of embryos analyzed.

(E) Images of the cortex in embryos expressing NMY-2::GFP. Numbers indicate the time in seconds after anaphase onset. Scale bars, 10 μm.

See also Video S2 and Tables S1 and S2.

PLST-1::GFP localized to bundles similar to LifeAct::RFP (Figure 3A and signal overlap in Figure 3B), SMA-1::spGFP dots decorated those bundles but did not overlap with PLST-1::mCherry nor NMY-2::mKate2 (Figure 3B). The expression level and localization pattern of endogenous SPC-1::GFP was comparable to that of SMA-1::spGFP, and immunofluorescence with affinity-purified anti-SMA-1 antibody confirmed SMA-1's dotty distribution and equatorial accumulation during cytokinesis (Figures 3C and 3D). We conclude that SMA-1 is expressed at low levels in the one-cell embryo, that PLST-1 and SMA-1 have distinct localizations within the actomyosin network, and that, consistent with a previous report in mouse embryonic fibroblasts in interphase, spectrins and actomyosin distinctly organize in space.[34]

Synergy between SMA-1 and PLST-1 does not require SMA-1's SH3 and PH domains

PLST-1 is a small protein whose only known function is F-actin crosslinking, whereas the much larger SMA-1 contains three functionally distinct domains: an N-terminal ABD, an Src homology-3 (SH3) domain, thought to be involved in signal transduction that is inserted between spectrin repeats in the N-terminal half, and a C-terminal PH domain, which mediates interactions with the plasma membrane. The remainder of the protein consists of spectrin repeats, which confer an elongated shape and flexibility, promote spectrin dimerization and tetramerization, and may mediate additional protein-protein interactions (Figures 2B and 4A).[17] To define the contribution of SMA-1 domains to the observed synergy between SMA-1 and PLST-1, we used genome editing to delete the regions encoding the SH3 domain (ΔSH3) and the PH domain (ΔPH) from the *sma-1* locus (Figure 4A). *sma-1 ΔSH3* and *sma-1 ΔPH* animals were viable, grew to normal adult size, and were fully fertile. This contrasts with *sma-1(ru18)* animals, which are small and have a reduced brood size.[23] Immunoblots with anti-SMA-1 antibodies showed that the expression levels of SMA-1ΔSH3 and SMA-1ΔPH were similar to wild-type SMA-1, while no detectable SMA-1 was expressed in the *sma-1(ru18)* mutant (Figure 4B).

We next crossed the *sma-1* domain mutants with the *plst-1(prt89)* mutant and obtained homozygous viable double mutants. Imaging of one-cell embryos expressing NMY-2::GFP showed that the percentage of cytokinesis failure remained low in *plst-1(prt89);sma-1 ΔSH3* and *plst-1(prt89);sma-1 ΔPH* (19% and 0%, respectively, versus 8% in *plst-1(prt89)*; Figures 4C and 4D).

Furthermore, cortical LifeAct::GFP and NMY-2::mCherry localization patterns in the single and double mutants were similar to those observed in controls and the *plst-1(prt89)* mutant, respectively (Figure 4E; Video S2). SMA-1 establishes interactions with the plasma membrane directly through its PH domain and indirectly through other membrane-localized proteins, namely, ankyrin, ezrin-radixin-moesin, and protein 4.1.[17] We therefore co-depleted ankyrin (UNC-44), ezrin-radixin-moesin (ERM-1), and protein 4.1 (FRM-1) by RNAi in *plst-1(prt89);sma-1ΔPH* embryos. The efficiency of the triple RNAi was validated by confirming: signal disappearance in a strain that expresses ERM-1::GFP, delayed hatching due to FRM-1 depletion, and decreased brood size due to UNC-44 depletion.[35–37] Cytokinesis successfully completed in 96% of triple-depleted *plst-1(prt89);sma-1ΔPH* embryos (Figure 4D). We conclude that neither the SH3 nor the PH domain of SMA-1 is required for the synergistic action between SMA-1 and PLST-1 during cytokinesis, which completes even when 3 additional membrane anchoring proteins are co-depleted in *sma-1ΔPH* embryos. Although we cannot rule out the possibility that the SH3 domain may play a role in linking SMA-1 to the plasma membrane, these results suggest that cytokinesis failure in the absence of PLST-1 and SMA-1 is unlikely due to problems in anchoring the F-actin cortex to the plasma membrane.

Co-inhibition of PLST-1 and SMA-1 results in the collapse of equatorial F-actin bundles

We next asked whether PLST-1 and SMA-1 synergize through their F-actin crosslinking activities. To generate a SMA-1 mutant defective in actin-binding, we sought to delete its CH domains (CH1 and CH2). Although numerous attempts failed to produce precise full deletions, we succeeded in obtaining multiple partial deletions. We chose two for further characterization: SMA-1ΔABD#1, which only retains the last 14 residues of CH2, and SMA-1ΔABD#2, which retains the first 17 residues of CH1 and the entire CH2 (Figure S2A). Both mutants phenocopied the *sma-1(ru18)* mutant: adult animals were small and had a reduced brood size, and embryos completed cytokinesis successfully. Similar to genetic crosses with *sma-1(ru18)*, homozygous *sma-1ΔABD#1;plst-1(prt89)* animals were unable to propagate, but in this case they laid more embryos (16 on average). These embryos did not hatch (91%) or arrested at the L1 stage (9%). Immunoblots with the antibody raised against the SMA-1 PH domain showed that protein levels were reduced in the two *sma-1ΔABD* mutants (Figure S2B), which complicated the interpretation of the phenotype. We therefore asked whether partial RNAi-mediated depletion of SMA-1 in *plst-1(prt89)* embryos, to levels comparable to those in *sma-1ΔABD* mutants, was per se sufficient to induce cytokinesis failure (Figure S2C). In contrast to penetrant *sma-1(RNAi)*, partial *sma-1(RNAi)* did not prevent cytokinesis in *plst-1(prt89)* one-cell embryos (Figure S2D). It is therefore likely that SMA-1's inability to bind actin contributes to the embryonic lethality in *plst-1(prt89);sma-1ΔABD* mutants.

To examine how SMA-1 contributes to cortical F-actin dynamics during cytokinesis, we imaged LifeAct::GFP. In one-cell control embryos, approximately 70 s after anaphase onset, and coincident with the beginning of equatorial deformation, circumferentially aligned F-actin bundles could be observed in the division plane (Figure 5A). The localization pattern of F-actin in *sma-1(RNAi)* embryos was indistinguishable from that in controls (Figures 5A and S5A). In *plst-1(prt89)* embryos, F-actin bundles took longer to align circumferentially (Figures 5A and 5C).[16] In *plst-1(prt89);sma-1(RNAi)* embryos, equatorial F-actin bundles initially attempted to align circumferentially, similar to F-actin bundles in *plst-1(prt89)* embryos, but became increasingly disorganized around the time of equatorial deformation (Figures 5B and 5C). At this time, bright actin clusters started to appear in the equatorial region, and their number increased over time (Figures 5A, 5B, 6C, S5A). These bright F-actin clusters were never observed in control or *sma-1(RNAi)* embryos and were only rarely observed in *plst-1(prt89)* embryos (Figures 5A and 6C). Strikingly, equatorial F-actin bundles had completely disappeared by 312 ± 64 s after anaphase onset, such that only F-actin clusters remained. Eventually, the equatorial deformation regressed 382 ± 82 s after anaphase onset (Figure 5A; Video S3). We conclude that co-inhibition of PLST-1 and SMA-1 severely disrupts the F-actin network at the cell equator, resulting in cytokinesis failure.

When astral microtubules of the mitotic spindle pull on a weakened actomyosin cortex, plasma membrane and cortical invaginations form.[38] Consistent with F-actin network collapse and consequent weakening of the cortex, we observed numerous invaginations when imaging the central plane in *plst-1(prt89);sma-1(RNAi)* embryos (Figures 5D–5F). These invaginations were observed from anaphase onset and became more frequent ~300 s later (Figure 5E), just prior to F-actin bundle collapse (Figure 6C). *plst-1(prt89)* embryos also presented invaginations, but these were less pronounced and much less frequent, and their number decreased as cytokinesis progressed. Mitotic spindle morphology and positioning was identical in control, *plst-1(prt89)*, and *plst-1(prt89);sma-1(RNAi)* embryos expressing GFP::β-tubulin (Figure S3), suggesting that the plasma membrane invaginations in *plst-1(prt89);sma-1(RNAi)* embryos were not caused by increased astral microtubule density or altered centrosome proximity to the cell cortex.

Directed F-actin cortical flows are a hallmark of early cytokinesis.[13,16,39] To assess whether perturbed F-actin cortical flows could contribute to cytokinesis failure in *plst-1(prt89);sma-1(RNAi)* embryos, we analyzed flows by Particle Image Velocimetry from anaphase onset in embryos expressing LifeAct::GFP (Figure S4). Posterior-anterior directed (X-component) flows in control embryos, which were particularly prominent on the posterior side, initiated before equatorial deformation and peaked shortly thereafter (Figures S4A and S4B). As described previously,[13,16] F-actin cortical flows in *plst-1(prt89)* embryos were erratic and decreased in velocity. The flow profile in *plst-1(prt89);sma-1(RNAi)* embryos was not further aggravated relative to that in *plst-1(prt89)* embryos. We also analyzed the Y-component flow profile and found it to be similar between *plst-1(prt89)* and *plst-1(prt89);sma-1(RNAi)* embryos (Figure S4C).[16] These results imply that the failure to form a contractile ring in *plst-1(prt89);sma-1(RNAi)* embryos is not attributable to impaired F-actin flows.

F-actin bundle collapse after co-inhibition of PLST-1 and SMA-1 coincides with the coalescence of myosin into large puncta

To further assess the status of the actomyosin network, we imaged the cortex of embryos co-expressing LifeAct::GFP and NMY-2::mCherry. Initially, the patchy equatorial NMY-2::mCherry distribution was similar in control and

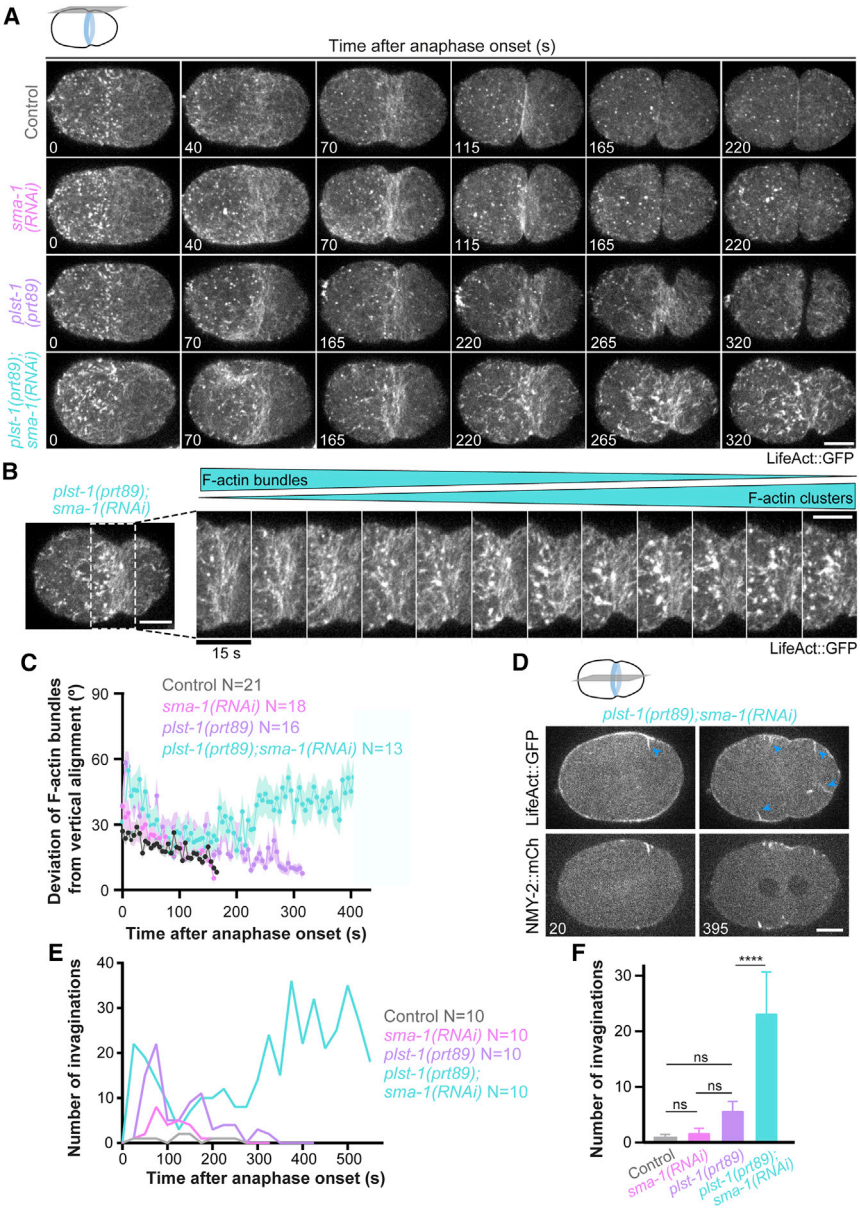

Figure 5. Co-inhibition of PLST-1 and SMA-1 results in collapse of F-actin bundles at the cell equator

(A) Images of the cortex in one-cell embryos expressing LifeAct::GFP. Numbers indicate the time in seconds after anaphase onset. Scale bar, 10 μm.

(B) Images of the equatorial region in a *plst-1(prt89);sma-1(RNAi)* embryo expressing LifeAct::GFP. The first frame corresponds to the time at which a distinct F-actin equatorial band has formed. Scale bars, 10 μm.

(C) Deviation of F-actin bundles from vertical alignment at the equatorial cortex versus time after anaphase onset (mean ± SEM).

(D) Images of the central plane in *plst-1(prt89);sma-1(RNAi)* embryos expressing LifeAct::GFP and NMY-2::mCherry. Numbers indicate the time in seconds after anaphase onset. Blue arrowheads point to membrane/cortex invaginations. Scale bar, 10 μm.

(E) Number of invaginations in the one-cell embryo during successive 25 s intervals after anaphase onset. For each time point the total number of invaginations observed in 10 embryos are plotted.

(F) Number of cortical invaginations in the one-cell embryo (mean ± 95% CI; 10 embryos) in a 400 s interval starting at anaphase onset. Statistical significance was determined using one-way ANOVA followed by Bonferroni's multiple comparison: ****$p \leq 0.0001$; ns, not significant ($p > 0.05$). See also Figures S2 and S5, Video S3, and Table S1.

plst-1(prt89);sma-1(RNAi) embryos. However, NMY-2::mCherry patches in *plst-1(prt89);sma-1(RNAi)* embryos quickly gave way to large, bright puncta (Figures 6A–6C and S5A). The appearance of NMY-2::mCherry puncta (~115 s after anaphase onset) coincided with the appearance of F-actin clusters, and they frequently co-localized (Figures 6B and 6C). The number of bright NMY-2::mCherry puncta increased as F-actin bundles disappeared from the cell equator and reached a maximum 320 s after anaphase onset, shortly after the complete collapse of F-actin bundles (Figures 5A, 5B, and 6C). The remaining faint patches of NMY-2::mCherry disappeared along with the F-actin bundles. At this time (382 ± 82 s after anaphase onset) all cortical NMY-2::mCherry was in the form of bright puncta, and the cortex relaxed. The number of NMY-2::mCherry puncta decreased thereafter and all puncta eventually disappeared around 550 s after anaphase onset. We conclude that the disintegration of F-actin bundles at the cell equator of *plst-1(prt89);sma-1(RNAi)* embryos coincides with a re-distribution of myosin from faint patches to bright puncta.

Myosin localization dynamics after co-inhibition of PLST-1 and SMA-1 resemble those observed after drug-induced F-actin depolymerization

Myosin puncta are known to form at the cell surface in embryos treated with Latrunculin A,[40] a drug that inhibits F-actin polymerization by sequestering actin monomers.[7] To assess the similarity between the myosin puncta in *plst-1(prt89);sma-1(RNAi)* embryos and those observed after Latrunculin A treatment, we permeabilized one-cell embryos co-expressing Lifeact::GFP and NMY-2:mCherry and acutely treated them with 10 μM Latrunculin A at anaphase onset.[41] As previously described, Latrunculin A treatment resulted in depolymerization of the cortical F-actin network and failure of cytokinesis (Figure 6D). Concomitant with F-actin depolymerization, NMY-2::mCherry accumulated in bright puncta at the cell surface, especially at the cell equator where the contractile ring would be assembled. These NMY-2::mCherry puncta were undistinguishable in brightness, size, and shape from those we observed in *plst-1(prt89);sma-1(RNAi)* embryos,

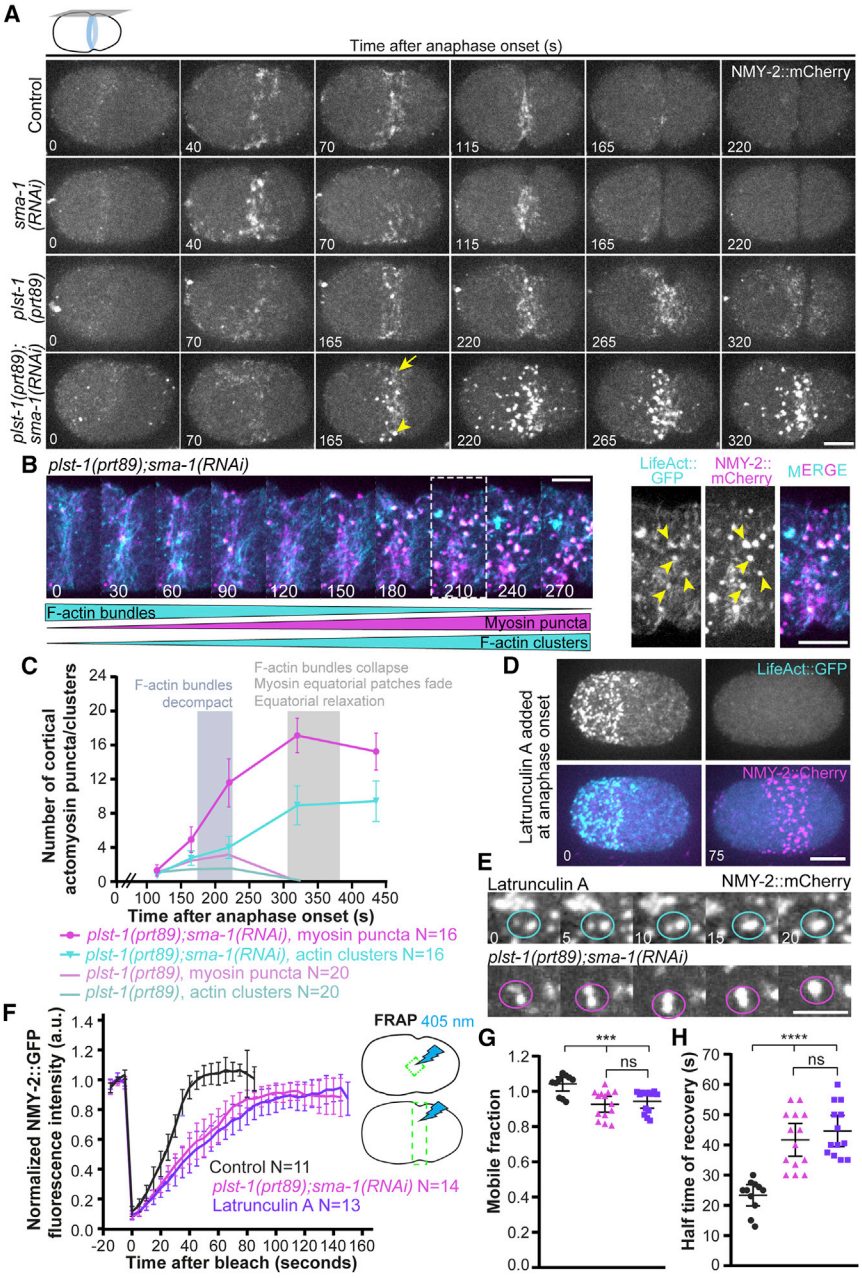

Figure 6. Co-inhibition of PLST-1 and SMA-1 leads to coalescence of equatorial myosin into large puncta, which behave identically to puncta that form after Latrunculin A treatment

(A) Images of the cortex in one-cell embryos expressing NMY-2::mCherry. Yellow arrows and arrowheads point to myosin patches and myosin puncta, respectively. Numbers indicate the time in seconds after anaphase onset. Scale bar, 10 μm.

(B) Images of the cortical equatorial region in a *plst-1(prt89);sma-1(RNAi)* embryo co-expressing NMY-2::mCherry and LifeAct::GFP. Numbers indicate the time in seconds after the initial enrichment of NMY-2::mCherry at the cell equator. A blow-up of the 210 s time point (outlined by a dashed line) is shown on the right. Arrowheads point to F-actin clusters and myosin puncta that co-localize. Scale bars, 10 μm.

(C) Quantification of the number of myosin puncta and F-actin clusters (mean ± 95% CI) over time after anaphase onset. N indicates the number of embryos analyzed.

(D) Images of the cortex in one-cell embryos co-expressing LifeAct::GFP and NMY-2::mCherry after acute treatment with 10 μM Latrunculin A. Numbers indicate the time in seconds after anaphase onset, when Latrunculin A was added. Scale bar, 10 μm.

(E) Cortical images of *plst-1(prt89);sma-1(RNAi)* and Latrunculin A-treated one-cell embryos expressing NMY-2::mCherry showing fusion of myosin puncta. Scale bar, 5 μm.

(F) Quantification of NMY-2::GFP fluorescence recovery after photobleaching (mean ± 95% CI). Values were normalized to the fluorescence before photobleaching. Results from photobleaching of the regions in the schematics on the right and of the regions shown in Figures S6A and S6B were combined. Dashed lines are the single exponential fitting curves from which the half time of recovery and mobile fraction were extrapolated. N indicates the number of bleaching events analyzed (one per embryo).

(G and H) Quantification of the mobile NMY-2::GFP fraction (G) and the NMY-2::GFP half time of recovery (H) (mean ± 95% CI). Statistical significance was determined using one-way ANOVA followed by Bonferroni's multiple comparison test: ***$p < 0.001$; ****$p < 0.0001$; ns, not significant ($p > 0.05$).

See also Figures S5 and S6, Video S3, and Table S1.

and in both conditions puncta occasionally fused with one another (Figure 6E).

We further examined the dynamics of myosin puncta by photobleaching regions of two different sizes at the cortical equator during contractile ring assembly in embryos expressing NMY-2::GFP (Figures S6A and S6B). Quantification of the NMY-2::GFP signal over time post-bleaching revealed a fast and full recovery in control embryos, with a half time of recovery of 23.3 ± 3.7 s. In contrast, recovery of the NMY-2::GFP signal was significantly slower in both Latrunculin A-treated and *plst-1(prt89);sma-1(RNAi)* embryos, with a half time of recovery of 44.6 ± 5.4 s and 41.7 ± 5.5 s, respectively. Signal recovery occurs mostly from the cytoplasm in *plst-1(prt89);sma-1(RNAi)* and Latrunculin A-treated embryos, as actomyosin cortical flows are essentially absent. In controls, it is possible that cortical flows contribute to signal recovery. We note, however, that the recovering signal at the cell equator does reach a plateau, which is not what would be expected if the bi-directional flows converging on the equator were driving recovery (in this case the signal should keep increasing). The mobile NMY-2::GFP fraction also decreased slightly in either condition (0.94 ± 0.05 and 0.93 ± 0.05 in Latrunculin A-treated and *plst-1(prt89);sma-1(RNAi)* embryos, respectively; Figures 6F–6H). Thus, Latrunculin A treatment and *plst-1(prt89);sma-1(RNAi)* have the same effect on cortical myosin turnover.

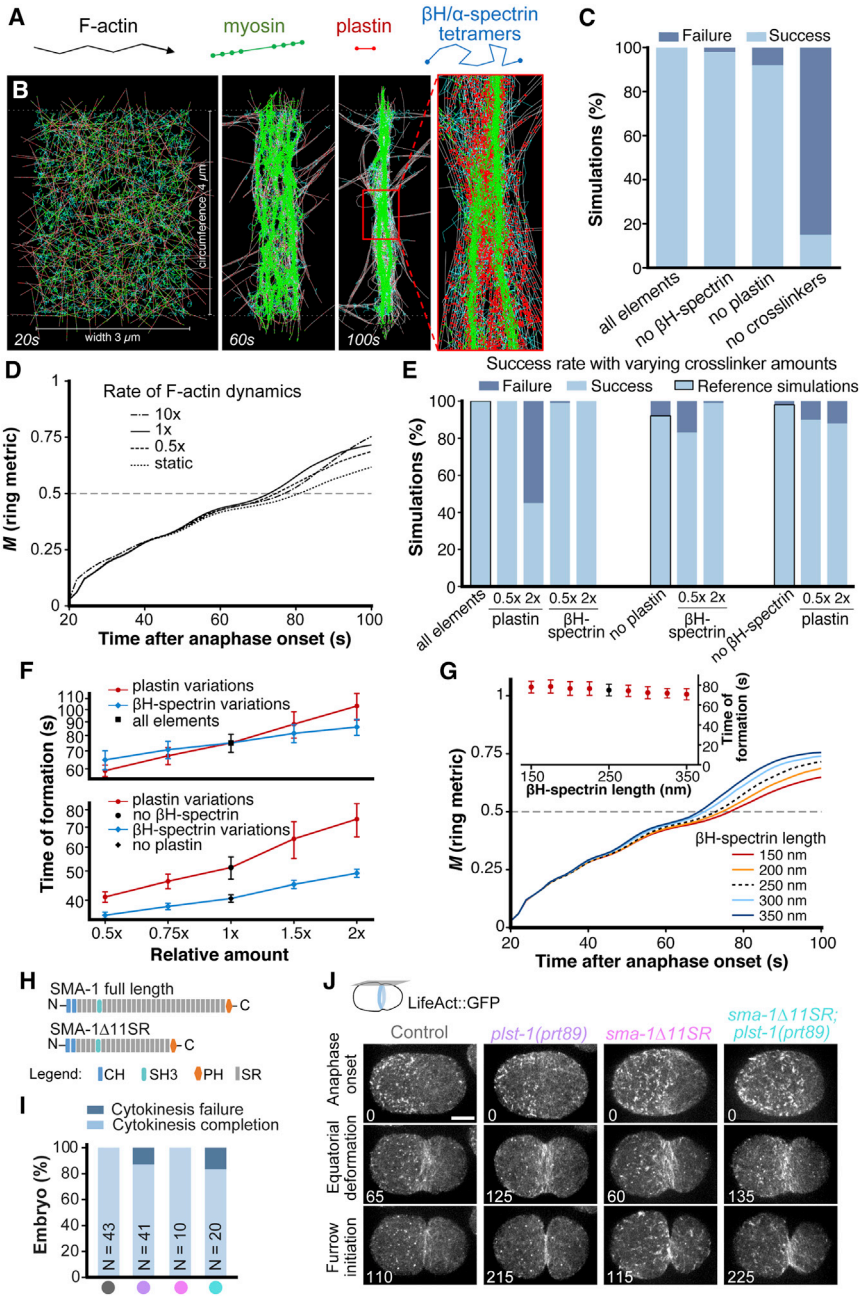

Figure 7. *In silico* simulations recapitulate contractile ring formation in the presence of a small and rigid and a large and flexible crosslinker

(A) The 4 cytoskeletal elements of the simulations (not to scale).

(B) Time series of ring formation for the reference simulation with all elements (white, actin fibers; green, myosin; red, plastin; blue, βH/α-spectrin tetramer). A blow-up of the marked region is shown to highlight vertical F-actin alignment.

(C) Success rate for different scenarios.

(D) Ring metric over time for the scenario with all elements for different F-actin dynamics. The inset shows the success rate for each scenario as a function of different F-actin dynamics.

(E) Success rate for higher (2×) and lower (0.5×) amounts of each crosslinker. Corresponding results with no crosslinker variation are shown with black borders for reference.

(F) Time of ring formation ± SD as a function of changes in the amount of each crosslinker (measured for the successful cases). Top: changes in timing relative to simulations with all elements present. Bottom: changes in timing relative to simulations where the other crosslinker is absent.

(G) Ring metric evolution for different lengths of βH-spectrin with all elements present. The inset shows the time of ring formation ± SD as a function of βH-spectrin length.

(H) Schematic of wild-type SMA-1 and SMA-1Δ11SR.

(I) Percentage of cytokinesis completion/failure in one-cell embryos. N indicates the number of embryos analyzed.

(J) Images of the cortex in embryos expressing LifeAct::GFP. Numbers indicate the time in seconds after anaphase onset. Scale bar, 10 μm.

See also Figure S7, Videos S2 and S4, and Tables S1–S3.

Collectively, our results support the idea that myosin puncta observed in the absence of PLST-1 and SMA-1 form as a consequence of F-actin bundle collapse at the cell equator. We conclude that the combined action of plastin and βH-spectrin is critical for maintenance of the cortical F-actin network that forms the contractile ring.

In silico simulations recapitulate contractile ring formation in the presence of a small and rigid and a large and flexible crosslinker

To gain insight into how plastin and βH-spectrin cooperate to stabilize the contractile ring, we developed an object/agent-based computational model for contractile ring formation using Cytosim. In our simulations, F-actin, myosin bipolar filaments, plastin, and βH-spectrin were individually represented in a 2D space that mimics the equatorial cortex of the *C. elegans* one-cell embryo (Figures 7A and 7B; Video S4; STAR Methods). F-actin was modeled as either static or dynamic; myosin filaments were modeled as rigid rods with heads that can independently bind and walk along F-actin and dwell at the barbed-end of filaments before unbinding;[42] each crosslinker consisted of two heads that bind to different actin filaments, and a connecting backbone, which is short and rigid for plastin (12 nm), and long and flexible for βH-spectrin (estimated to be about 250 nm when stretched).

To test whether the combination of these 4 cytoskeletal elements could recreate contractile ring formation, we defined the metric *M* for successful ring assembly based on the distribution of the motors along the ring network (Figure S7B). *M* varied between one, when motors move toward the middle of the

simulated space horizontally and uniformly spread across the vertical parallel to the actin filaments, and zero, when the ring network ruptures because of connectivity loss, and the motors contract the network into clusters (Figure S7B; STAR Methods). By comparing our metric to videos of simulations, we determined that a ring has successfully formed if *M* exceeds a threshold value of 0.5. Using this threshold, we calibrated our simulations to the four scenarios: all 4 elements, no βH-spectrin, no plastin, and neither βH-spectrin nor plastin (no crosslinkers). Similar to our experimental results (Figure 2A), the success rate of ring formation was 100%, 98%, 92%, and 15% in the four scenarios, respectively (Figures 7C and S7E–S7H). In the 4 elements scenario, the calibrated system also recapitulated the time interval of contractile ring formation (average 55 s, range 20 s to 75 s; Figure 7D), which is similar to the interval between equatorial actin enrichment (~20 s after anaphase onset, Video S3) and equatorial deformation, when F-actin bundles are already aligned (Figure 5A). The calibration was possible when the number of plastin connectors was at least one order of magnitude higher than the number of βH-spectrins (Table S3), which is consistent with the higher signal of PLST-1::GFP relative to that of SMA-1::spGFP or SPC-1::GFP (Figure S7A). Changes in the polymerization and depolymerization rates of actin filament ends had little impact on timing of ring assembly or success rate in the 4-element scenario (Figure 7D).

Doubling the amount of plastin had adverse effects on the success rates, while halving its amount only affected simulations with no βH-spectrins. Changes in the amounts of βH-spectrins did not affect the success rate when all elements are present, but halving it did affect the success rate in the absence of plastin (Figure 7E). An excess of either crosslinker in the 4-element scenario slowed down ring formation times, which is in agreement with previous reports that relate increased network connectivity to decreased contractility.[13,43] Interestingly, increasing plastin in the absence of spectrin or vice versa also led to an increase in ring formation time, indicating that one crosslinker does not compensate for the other. Decreasing the amount of either crosslinker to 75% or 50% sped up ring formation time (Figure 7F). The likely reason for this is that, as long as there is some level of F-actin connectivity, and in the absence of anchoring to a plasma membrane and of other actomyosin regulators that could provide drag, it is easier for motors to align the ring network.

The main difference between SMA-1 and UNC-70 structure is the number of spectrin repeats that confers different lengths to the two molecules. To test whether the length of SMA-1 is important for its function during cytokinesis, we simulated ring assembly in the presence of βH-spectrin that ranged from half to double its estimated length of 250 nm and concluded that within this range βH-spectrin length had negligible effects on success rate and timing of ring formation (Figure 7G; Video S4). This is in agreement with results we obtained *in vivo* with a truncated version of SMA-1 that lacks 11 of its 29 spectrin repeats (SMA-1Δ11SR; Figure 7H). SMA-1Δ11SR is approximately the same length as UNC-70, which contains 17 spectrin repeats. Animals expressing SMA-1Δ11SR were viable, cytokinesis in one-cell embryos was normal, and expression of SMA-1Δ11SR in the *plst-1(prt89)* background neither aggravated the time required for ring formation nor the success rate of cytokinesis (Figures 7I and 7J). We conclude that the difference in length between the two β-spectrins is not a critical parameter for SMA-1's cooperation with plastin.

DISCUSSION

Studies *in vitro* and theoretical approaches suggest that F-actin crosslinking is critical for tension propagation and contractility of actomyosin networks,[13,43,44] yet the role of F-actin crosslinkers *in vivo* remains poorly understood. We determined the contributions of nine conserved crosslinkers to embryonic cytokinesis in *C. elegans* and found that none of them are essential when inhibited individually. Inhibition of the plastin homolog PLST-1, which has previously been implicated in cytokinesis, delays contractile ring assembly but does not affect the speed of ring closure.[13,16] In the sensitized plastin inhibition background, the βH-spectrin SMA-1, but none of the other crosslinkers we examined, becomes essential for cytokinesis. Our findings indicate that interplay between plastin and βH/α-spectrin occurs via their actin-binding activities and does not involve SMA-1's plasma membrane anchoring function. Thus, two types of F-actin crosslinker with distinct properties collaborate in actomyosin network organization during cytokinesis. The only previous hint that spectrins may have a role in animal cell division comes from work in *D. melanogaster* ovaries, where α-spectrin-deficient cysts were found to have fewer cells.[45] Of note, cell division in bacteria involves the spectrin-like protein EzrA, which may contribute to the condensation of the tubulin FtsZ (tubulin-homolog) filaments that compose the cytokinetic Z-ring.[46] However, EzrA is a small protein of 65 kDa that only contains five spectrin-like repeats and lacks an ABD, implying a different function from that of SMA-1 that we report here.

The small (9–12 nm) and rigid plastin, whose main structural feature are two ABDs in tandem, organizes non-branched F-actin in tight, parallel bundles.[6,12,13,47] By contrast, conventional spectrin tetramers are large and flexible (an estimated 80 nm when relaxed and 200 nm when extended).[17,48] β-spectrins contain up to 30 spectrin repeats linked by flexible loops. Unfolding of the spectrin repeats under shear stress allows for spectrin extension, which provides red blood cells with the ability to deform when crossing blood vessels.[17] In axons, spectrins provide protection from mechanical stress, caused, for example, by animal movement in *C. elegans*.[49] In *C. elegans*, spectrins are also required for F-actin bundle organization and reinforcement during the cycles of stretching and contraction in the spermatheca, where oocytes enter to be fertilized before being expelled into the uterus,[50] and spectrins help stabilize F-actin bundles in epidermal cells, allowing for their remodeling when muscle cells contract during embryo elongation.[51] Whether βH-spectrin is under tension during cytokinesis and whether it offers mechanical protection to the cell equator remains to be investigated.

PLST-1 is clearly bundling equatorial F-actin, as its signal and that of LifeAct overlap. In contrast, SMA-1 appears to fill the spaces between F-actin bundles, which supports the idea that the two crosslinkers make distinct contributions to the stability of the contractile ring. Super-resolution microscopy will be required to better understand SMA-1's distribution within the actomyosin network. In our *in silico* model, successful ring formation requires that plastin is one order of magnitude more

abundant than spectrin, and, while either crosslinker is sufficient for actomyosin ring formation, plastin must still be more abundant than spectrin in these scenarios. This requirement probably reflects the size difference between plastin and spectrin: the compact plastin can only crosslink actin filaments that are already in close proximity, whereas the approximately 20 times longer βH/α-spectrin can crosslink filaments at much greater distance. Variations in the absolute amounts of βH/α-spectrin had negligible effects in our simulations, but doubling plastin adversely affected ring formation success rate in the absence of βH/α-spectrin. This is because an excess of plastin stiffens the network and stalls the motors, whereas too much spectrin, because of its length and flexibility, still allows the network to be remodeled.

An interesting open question is why the βH-spectrin SMA-1 is used for cytokinesis and not the conventional β-spectrin UNC-70, whose expression in the early embryo appears to be negligible (GFP-tagged endogenous expression is not detectable on the cortex,[21] and only a feeble signal is detected by immunofluorescence at the cell-cell boundary of the 2-cell embryo[26]). The most obvious difference between βH-spectrin and conventional β-spectrin is length, but our simulations and *in vivo* results with truncated SMA-1, which contains only one more spectrin repeat than UNC-70, argue against this being an important factor. Another feature that distinguishes the two β-spectrins is the ability to respond to mechanical stress: βH-spectrin is mechanosensing in micropipette aspiration assays in S2 cells, whereas conventional β-spectrin is not.[22] βH-spectrin's mechanosensing behavior explains its recruitment to the fusion site of myoblasts in *Drosophila* in response to the transient increase in protrusive forces by the attacking cell.[22] At that site, βH/α-spectrin keeps cell-adhesion molecules fenced and serves as a sieve to focus the protrusions of the attacking cell, facilitating the fusion event. In the context of cytokinesis, mechanosensing could potentially allow the βH-spectrin SMA-1 to detect tension at the cell equator that builds due to myosin recruitment, thereby facilitating local spectrin accumulation. If mechanosensing by βH-spectrin is important for cytokinesis, UNC-70 may not be able to functionally replace SMA-1. Unfortunately, we have not been able to test this, as efforts to force transgenic UNC-70 expression in the one-cell embryo have been unsuccessful, presumably due to the well-documented potency of silencing mechanisms that operate in the *C. elegans* germline.

Our analysis of myosin and F-actin dynamics shows that the equatorial actomyosin network progressively disintegrates in the absence of βH-spectrin and plastin. It is known that myosin can remodel isotropic F-actin meshworks into asters *in vitro* because myosin filaments dwell at F-actin plus ends, which results in plus-end clustering.[42,52] Addition of α-actinin leads to the stabilization of asters, which become larger, interconnected, and able to move toward one another until they merge.[42] In SMA-1 and PLST-1 co-inhibited embryos, it is possible that equatorial F-actin orientation becomes randomized and that the end-dwelling behavior of NMY-2 drives its coalescence into clusters of F-actin plus-ends. Lack of interconnectivity between these clusters would then prevent network contraction. In addition, F-actin itself is likely to become destabilized in the absence of βH-spectrin and plastin, since we show that the bright cortical myosin puncta resemble those that form after Latrunculin A treatment.[40]

In this view, the roles of βH-spectrin and plastin during cytokinesis go beyond mere crosslinking. Several crosslinkers have been reported to stabilize F-actin *in vitro* by decreasing its depolymerization rate and, in some instances, by concomitantly increasing the elongation rate or decreasing access to the severing protein cofilin.[53–55] There is also *in vivo* evidence for F-actin stabilization by crosslinkers: plastin stabilizes actin patches in yeast, espin stabilizes and lengthens F-actin bundles in microvilli of epithelial cultured cells and in stereocilia in hair cells, and fascin and forked stabilize bristles in *D. melanogaster*.[53,56,57] During contractile ring assembly in cytokinesis, when formin-mediated F-actin elongation occurs concomitantly with alignment and compaction of F-actin bundles, a dual ability to crosslink and stabilize F-actin would appear to be advantageous. Following contractile ring assembly, however, contractile ring constriction requires F-actin depolymerization.[58,59] This raises the question of whether the F-actin crosslinking and stabilization activities of SMA-1 and PLST-1 might be regulated to facilitate F-actin depolymerization during ring constriction. In the future, it will be important to investigate how the cooperation between plastin and spectrin impacts F-actin network dynamics *in vitro*, including in the presence/absence of cofilin, which would allow further refinement of our *in silico* model.

Our findings highlight the importance of exploring how interplay between crosslinkers of variable size, flexibility, and mechanical properties contribute to actomyosin network contractility and stability. For cytokinesis, we envision the following sequence of events: equatorial plastin promotes myosin motor-driven F-actin alignment through F-actin bundling as well as stabilization, the latter possibly involving inhibition of F-actin depolymerization or restriction of cofilin access to F-actin. As tension builds at the cell equator because of continuous myosin recruitment, βH-spectrin accumulates locally due to its mechanosensing properties and helps protect the circumferential F-actin bundle array from mechanical stress. It will be interesting to test this model using additional engineered plastin and spectrin mutants and to investigate potential roles of the plastin/βH-spectrin pair and other crosslinker combinations in actomyosin-dependent processes beyond cytokinesis.

STAR★METHODS

Detailed methods are provided in the online version of this paper and include the following:

- KEY RESOURCES TABLE
- RESOURCE AVAILABILITY
  - Lead contact
  - Materials availability
  - Data and code availability
- EXPERIMENTAL MODEL AND SUBJECT DETAILS
  - *C. elegans* strains
- METHOD DETAILS
  - RNA interference
  - Generation of mutants using CRISPR/Cas9
  - Tagging of endogenous SMA-1 and PLST-1
  - Live imaging
  - Image processing
  - Latrunculin A treatment

- Generation of antibodies against SMA-1
- Protein extracts and immunoblotting
- Immunofluorescence
- Computational simulations

- QUANTIFICATION AND STATISTICAL ANALYSIS
  - Image quantifications
  - Actin cortical flows
  - FRAP
- STATISTICAL ANALYSIS

SUPPLEMENTAL INFORMATION

Supplemental information can be found online at https://doi.org/10.1016/j.cub.2021.09.055.

ACKNOWLEDGMENTS

We thank Arshad Desai, Ronen Zaidel-Bar, Guangshuo Ou, Mike Boxem, and Julien Dumont for strains. Some strains were provided by the CGC, which is funded by NIH Office of Research Infrastructure Programs (P40 OD010440). The research leading to these results was funded by the European Research Council under the European Union's Horizon 2020 Research and Innovation Programme (grant agreement 640553 – ACTOMYO). A.X.C. and R.G. are supported by Principal Investigator positions from FCT (CEECIND/01967/2017 and CEECIND/00333/2017, respectively). J.M.B. and M.J.N. are supported by NCSU. F.-Y.C. and D.J.B. are supported by FCT junior researcher positions (DL 57/2016/CP1355/CT0013 and DL57/2016/CP1355/CT0007) and A.F.S. by an FCT PhD scholarship (SFRH/BD/121874/2016). The funders had no role in study design, data collection and analysis, decision to publish, or preparation of the manuscript.

AUTHOR CONTRIBUTIONS

Conceptualization, A.X.C.; investigation and formal analysis, A.F.S., F.-Y.C., M.J.N., A.B.D., and V.F.; methodology, A.F.S., F.-Y.C., M.J.N., D.S.O., D.J.B., and A.B.D.; writing – original draft, A.F.S., F-Y.C., J.M.B., and A.X.C.; writing – review & editing, A.F.S., F-Y.C., R.G., J.M.B., and A.X.C.; made strain OD4016, D.C.; supervision, A.X.C., R.G., and J.M.B.; funding acquisition, A.X.C. and J.M.B.

DECLARATION OF INTERESTS

The authors declare no competing interests.

Received: February 3, 2021
Revised: June 22, 2021
Accepted: September 21, 2021
Published: October 18, 2021

REFERENCES

1. Blanchoin, L., Boujemaa-Paterski, R., Sykes, C., and Plastino, J. (2014). Actin dynamics, architecture, and mechanics in cell motility. Physiol. Rev. *94*, 235–263.
2. Lieleg, O., Claessens, M.M.A., and Bausch, A.R. (2010). Structure and dynamics of cross-linked actin networks. Soft Matter *6*, 218–225.
3. Wachsstock, D.H., Schwartz, W.H., and Pollard, T.D. (1993). Affinity of α-actinin for actin determines the structure and mechanical properties of actin filament gels. Biophys. J. *65*, 205–214.
4. Flanagan, L.A., Chou, J., Falet, H., Neujahr, R., Hartwig, J.H., and Stossel, T.P. (2001). Filamin A, the Arp2/3 complex, and the morphology and function of cortical actin filaments in human melanoma cells. J. Cell Biol. *155*, 511–517.
5. Pan, L., Yan, R., Li, W., and Xu, K. (2018). Super-resolution microscopy reveals the native ultrastructure of the erythrocyte cytoskeleton. Cell Rep. *22*, 1151–1158.
6. Glenney, J.R., Jr., Kaulfus, P., Matsudaira, P., and Weber, K. (1981). F-actin binding and bundling properties of fimbrin, a major cytoskeletal protein of microvillus core filaments. J. Biol. Chem. *256*, 9283–9288.
7. Leite, J., Osorio, D.S., Sobral, A.F., Silva, A.M., and Carvalho, A.X. (2019). Network contractility during cytokinesis - from molecular to global views. Biomolecules *9*, 194.
8. Faix, J., Steinmetz, M., Boves, H., Kammerer, R.A., Lottspeich, F., Mintert, U., Murphy, J., Stock, A., Aebi, U., and Gerisch, G. (1996). Cortexillins, major determinants of cell shape and size, are actin-bundling proteins with a parallel coiled-coil tail. Cell *86*, 631–642.
9. Jananji, S., Risi, C., Lindamulage, I.K.S., Picard, L.-P., Van Sciver, R., Laflamme, G., Albaghjati, A., Hickson, G.R.X., Kwok, B.H., and Galkin, V.E. (2017). Multimodal and polymorphic interactions between anillin and actin: their implications for cytokinesis. J. Mol. Biol. *429*, 715–731.
10. Piekny, A.J., and Glotzer, M. (2008). Anillin is a scaffold protein that links RhoA, actin, and myosin during cytokinesis. Curr. Biol. *18*, 30–36.
11. Wu, J.Q., Bähler, J., and Pringle, J.R. (2001). Roles of a fimbrin and an α-actinin-like protein in fission yeast cell polarization and cytokinesis. Mol. Biol. Cell *12*, 1061–1077.
12. Matsudaira, P., Mandelkow, E., Renner, W., Hesterberg, L.K., and Weber, K. (1983). Role of fimbrin and villin in determining the interfilament distances of actin bundles. Nature *301*, 209–214.
13. Ding, W.Y., Ong, H.T., Hara, Y., Wongsantichon, J., Toyama, Y., Robinson, R.C., Nédélec, F., and Zaidel-Bar, R. (2017). Plastin increases cortical connectivity to facilitate robust polarization and timely cytokinesis. J. Cell Biol. *216*, 1371–1386.
14. Shinomiya, H. (2012). Plastin family of actin-bundling proteins: its functions in leukocytes, neurons, intestines, and cancer. Int. J. Cell Biol. *2012*, 213492.
15. Delanote, V., Vandekerckhove, J., and Gettemans, J. (2005). Plastins: versatile modulators of actin organization in (patho)physiological cellular processes. Acta Pharmacol. Sin. *26*, 769–779.
16. Leite, J., Chan, F.-Y., Osório, D.S., Saramago, J., Sobral, A.F., Silva, A.M., Gassmann, R., and Carvalho, A.X. (2020). Equatorial non-muscle myosin II and plastin cooperate to align and compact F-actin bundles in the cytokinetic ring. Front. Cell Dev. Biol. *8*, 573393.
17. Machnicka, B., Czogalla, A., Hryniewicz-Jankowska, A., Bogusławska, D.M., Grochowalska, R., Heger, E., and Sikorski, A.F. (2014). Spectrins: a structural platform for stabilization and activation of membrane channels, receptors and transporters. Biochim. Biophys. Acta *1838*, 620–634.
18. Machnicka, B., Grochowalska, R., Bogusławska, D.M., Sikorski, A.F., and Lecomte, M.C. (2012). Spectrin-based skeleton as an actor in cell signaling. Cell. Mol. Life Sci. *69*, 191–201.
19. Xu, K., Zhong, G., and Zhuang, X. (2013). Actin, spectrin, and associated proteins form a periodic cytoskeletal structure in axons. Science *339*, 452–456.
20. Krieg, M., Dunn, A.R., and Goodman, M.B. (2014). Mechanical control of the sense of touch by β-spectrin. Nat. Cell Biol. *16*, 224–233.
21. Jia, R., Li, D., Li, M., Chai, Y., Liu, Y., Xie, Z., Shao, W., Xie, C., Li, L., Huang, X., et al. (2019). Spectrin-based membrane skeleton supports ciliogenesis. PLoS Biol. *17*, e3000369.
22. Duan, R., Kim, J.H., Shilagardi, K., Schiffhauer, E.S., Lee, D.M., Son, S., Li, S., Thomas, C., Luo, T., Fletcher, D.A., et al. (2018). Spectrin is a mechanoresponsive protein shaping fusogenic synapse architecture during myoblast fusion. Nat. Cell Biol. *20*, 688–698.
23. McKeown, C., Praitis, V., and Austin, J. (1998). Sma-1 encodes a betaH-spectrin homolog required for *Caenorhabditis elegans morphogenesis*. Development *125*, 2087–2098.
24. Zarnescu, D.C., and Thomas, G.H. (1999). Apical spectrin is essential for epithelial morphogenesis but not apicobasal polarity in Drosophila. J. Cell Biol. *146*, 1075–1086.
25. Norman, K.R., and Moerman, D.G. (2002). α spectrin is essential for morphogenesis and body wall muscle formation in *Caenorhabditis elegans*. J. Cell Biol. *157*, 665–677.

CellPress
OPEN ACCESS

26. Moorthy, S., Chen, L., and Bennett, V. (2000). *Caenorhabditis elegans* β-G spectrin is dispensable for establishment of epithelial polarity, but essential for muscular and neuronal function. J. Cell Biol. *149*, 915–930.

27. Janji, B., Giganti, A., De Corte, V., Catillon, M., Bruyneel, E., Lentz, D., Plastino, J., Gettemans, J., and Friederich, E. (2006). Phosphorylation on Ser5 increases the F-actin-binding activity of L-plastin and promotes its targeting to sites of actin assembly in cells. J. Cell Sci. *119*, 1947–1960.

28. Meyer, R.K., and Aebi, U. (1990). Bundling of actin filaments by α-actinin depends on its molecular length. J. Cell Biol. *110*, 2013–2024.

29. Goode, B.L., Wong, J.J., Butty, A.C., Peter, M., McCormack, A.L., Yates, J.R., Drubin, D.G., and Barnes, G. (1999). Coronin promotes the rapid assembly and cross-linking of actin filaments and may link the actin and microtubule cytoskeletons in yeast. J. Cell Biol. *144*, 83–98.

30. Mavrakis, M., Azou-Gros, Y., Tsai, F.-C., Alvarado, J., Bertin, A., Iv, F., Kress, A., Brasselet, S., Koenderink, G.H., and Lecuit, T. (2014). Septins promote F-actin ring formation by crosslinking actin filaments into curved bundles. Nat. Cell Biol. *16*, 322–334.

31. Brown, J.W., Bullitt, E., Sriswasdi, S., Harper, S., Speicher, D.W., and McKnight, C.J. (2015). The physiological molecular shape of spectrin: a compact supercoil resembling a chinese finger trap. PLoS Comput. Biol. *11*, e1004302.

32. Nakamura, F., Osborn, T.M., Hartemink, C.A., Hartwig, J.H., and Stossel, T.P. (2007). Structural basis of filamin A functions. J. Cell Biol. *179*, 1011–1025.

33. Kamiyama, D., Sekine, S., Barsi-Rhyne, B., Hu, J., Chen, B., Gilbert, L.A., Ishikawa, H., Leonetti, M.D., Marshall, W.F., Weissman, J.S., and Huang, B. (2016). Versatile protein tagging in cells with split fluorescent protein. Nat. Commun. *7*, 11046.

34. Ghisleni, A., Galli, C., Monzo, P., Ascione, F., Fardin, M.-A., Scita, G., Li, Q., Maiuri, P., and Gauthier, N.C. (2020). Complementary mesoscale dynamics of spectrin and acto-myosin shape membrane territories during mechanoresponse. Nat. Commun. *11*, 5108.

35. Ramalho, J.J., Sepers, J.J., Nicolle, O., Schmidt, R., Cravo, J., Michaux, G., and Boxem, M. (2020). C-terminal phosphorylation modulates ERM-1 localization and dynamics to control cortical actin organization and support lumen formation during *Caenorhabditis elegans* development. Development *147*, dev188011.

36. Skop, A.R., Liu, H., Yates, J., 3rd, Meyer, B.J., and Heald, R. (2004). Dissection of the mammalian midbody proteome reveals conserved cytokinesis mechanisms. Science *305*, 61–66.

37. Choi, B., Kang, J., Park, Y.-S., Lee, J., and Cho, N.J. (2011). A possible role for FRM-1, a *C. elegans* FERM family protein, in embryonic development. Mol. Cells *31*, 455–459.

38. Redemann, S., Pecreaux, J., Goehring, N.W., Khairy, K., Stelzer, E.H.K., Hyman, A.A., et al. (2010). Membrane invaginations reveal cortical sites that pull on mitotic spindles in one-cell *C. elegans* embryos. PLoS ONE *5*, e12301.

39. Reymann, A.-C., Staniscia, F., Erzberger, A., Salbreux, G., and Grill, S.W. (2016). Cortical flow aligns actin filaments to form a furrow. eLife *5*, e17807.

40. Michaux, J.B., Robin, F.B., McFadden, W.M., and Munro, E.M. (2018). Excitable RhoA dynamics drive pulsed contractions in the early *C. elegans* embryo. J. Cell Biol. *217*, 4230–4252.

41. Carvalho, A., Olson, S.K., Gutierrez, E., Zhang, K., Noble, L.B., Zanin, E., et al. (2011). Acute drug treatment in the early *C. elegans* embryo. PLoS ONE *6*, e24656.

42. Wollrab, V., Belmonte, J.M., Baldauf, L., Leptin, M., Nédeléc, F., and Koenderink, G.H. (2018). Polarity sorting drives remodeling of actin-myosin networks. J. Cell Sci. *132*, jcs219717.

43. Ennomani, H., Letort, G., Guérin, C., Martiel, J.-L., Cao, W., Nédélec, F., De La Cruz, E.M., Théry, M., and Blanchoin, L. (2016). Architecture and connectivity govern actin network contractility. Curr. Biol. *26*, 616–626.

44. Stam, S., Freedman, S.L., Banerjee, S., Weirich, K.L., Dinner, A.R., and Gardel, M.L. (2017). Filament rigidity and connectivity tune the deformation modes of active biopolymer networks. Proc. Natl. Acad. Sci. USA *114*, E10037–E10045.

45. de Cuevas, M., Lee, J.K., and Spradling, A.C. (1996). α-spectrin is required for germline cell division and differentiation in the Drosophila ovary. Development *122*, 3959–3968.

46. Squyres, G.R., Holmes, M.J., Barger, S.R., Pennycook, B.R., Ryan, J., Yan, V.T., and Garner, E.C. (2021). Single-molecule imaging reveals that Z-ring condensation is essential for cell division in Bacillus subtilis. Nat. Microbiol. *6*, 553–562.

47. Volkmann, N., DeRosier, D., Matsudaira, P., and Hanein, D. (2001). An atomic model of actin filaments cross-linked by fimbrin and its implications for bundle assembly and function. J. Cell Biol. *153*, 947–956.

48. Byers, T.J., and Branton, D. (1985). Visualization of the protein associations in the erythrocyte membrane skeleton. Proc. Natl. Acad. Sci. USA *82*, 6153–6157.

49. Hammarlund, M., Jorgensen, E.M., and Bastiani, M.J. (2007). Axons break in animals lacking beta-spectrin. J. Cell Biol. *176*, 269–275.

50. Wirshing, A.C.E., and Cram, E.J. (2018). Spectrin regulates cell contractility through production and maintenance of actin bundles in the *Caenorhabditis elegans* spermatheca. Mol. Biol. Cell *29*, 2433–2449.

51. Lardennois, A., Pásti, G., Ferraro, T., Llense, F., Mahou, P., Pontabry, J., Rodriguez, D., Kim, S., Ono, S., Beaurepaire, E., et al. (2019). An actin-based viscoplastic lock ensures progressive body-axis elongation. Nature *573*, 266–270.

52. Verkhovsky, A.B., Svitkina, T.M., and Borisy, G.G. (1997). Polarity sorting of actin filaments in cytochalasin-treated fibroblasts. J. Cell Sci. *110*, 1693–1704.

53. Loomis, P.A., Zheng, L., Sekerková, G., Changyaleket, B., Mugnaini, E., and Bartles, J.R. (2003). Espin cross-links cause the elongation of microvillus-type parallel actin bundles in vivo. J. Cell Biol. *163*, 1045–1055.

54. Giganti, A., Plastino, J., Janji, B., Van Troys, M., Lentz, D., Ampe, C., Sykes, C., and Friederich, E. (2005). Actin-filament cross-linking protein T-plastin increases Arp2/3-mediated actin-based movement. J. Cell Sci. *118*, 1255–1265.

55. Schmoller, K.M., Semmrich, C., and Bausch, A.R. (2011). Slow down of actin depolymerization by cross-linking molecules. J. Struct. Biol. *173*, 350–357.

56. Tilney, L.G., Connelly, P.S., Ruggiero, L., Vranich, K.A., and Guild, G.M. (2003). Actin filament turnover regulated by cross-linking accounts for the size, shape, location, and number of actin bundles in Drosophila bristles. Mol. Biol. Cell *14*, 3953–3966.

57. Young, M.E., Cooper, J.A., and Bridgman, P.C. (2004). Yeast actin patches are networks of branched actin filaments. J. Cell Biol. *166*, 629–635.

58. Osório, D.S., Chan, F.-Y., Saramago, J., Leite, J., Silva, A.M., Sobral, A.F., Gassmann, R., and Carvalho, A.X. (2019). Crosslinking activity of non-muscle myosin II is not sufficient for embryonic cytokinesis in *C. elegans*. Development *146*, dev179150.

59. Mendes Pinto, I., Rubinstein, B., Kucharavy, A., Unruh, J.R., and Li, R. (2012). Actin depolymerization drives actomyosin ring contraction during budding yeast cytokinesis. Dev. Cell *22*, 1247–1260.

60. Schindelin, J., Arganda-Carreras, I., Frise, E., Kaynig, V., Longair, M., Pietzsch, T., Preibisch, S., Rueden, C., Saalfeld, S., Schmid, B., et al. (2012). Fiji: an open-source platform for biological-image analysis. Nat. Methods *9*, 676–682.

61. Nédélec, F., and Foethke, D. (2007). Collective Langevin dynamics of flexible cytoskeletal fibers. New J. Phys. *9*, 427.

62. Dickinson, D.J., Ward, J.D., Reiner, D.J., and Goldstein, B. (2013). Engineering the *Caenorhabditis elegans* genome using Cas9-triggered homologous recombination. Nat. Methods *10*, 1028–1034.

63. Dokshin, G.A., Ghanta, K.S., Piscopo, K.M., and Mello, C.C. (2018). Robust genome editing with short single-stranded and long, partially

single-stranded DNA donors in *Caenorhabditis elegans*. Genetics *210*, 781–787.

64. Arribere, J.A., Bell, R.T., Fu, B.X.H., Artiles, K.L., Hartman, P.S., and Fire, A.Z. (2014). Efficient marker-free recovery of custom genetic modifications with CRISPR/Cas9 in *Caenorhabditis elegans*. Genetics *198*, 837–846.

65. Gibson, D.G., Young, L., Chuang, R.-Y., Venter, J.C., Hutchison, C.A., 3rd, and Smith, H.O. (2009). Enzymatic assembly of DNA molecules up to several hundred kilobases. Nat. Methods *6*, 343–345.

66. Bidone, T.C., Jung, W., Maruri, D., Borau, C., Kamm, R.D., and Kim, T. (2017). Morphological transformation and force generation of active cytoskeletal networks. PLoS Comput. Biol. *13*, e1005277.

STAR★METHODS

KEY RESOURCES TABLE

REAGENT OR RESOURCE	SOURCE	IDENTIFIER
Antibodies		
Mouse monoclonal anti-α-tubulin	Sigma-Aldrich	Cat#T6199; RRID: AB_477583
Rabbit polyclonal anti-SMA-1 ABD	This paper	N/A
Rabbit polyclonal anti-SMA-1 PH	This paper	N/A
Goat anti-rabbit IgG secondary HRP-linked	Jackson ImmunoResearch	Cat#111-035-003; RRID: AB_2313567
Goat anti-mouse IgG secondary HRP-linked	Jackson ImmunoResearch	Cat#115-035-003; RRID: AB_10015289
Donkey anti-rabbit IgG secondary labeled with Alexa Fluor 488	Jackson ImmunoResearch	Cat#711-545-152; RRID: AB_2313584
Donkey anti-mouse IgG secondary labeled with Alexa Fluor 594	Jackson ImmunoResearch	Cat#715-585-150; RRID: AB_2340854
Bacterial and virus strains		
E. coli OP50 *C. elegans* food source	Caenorhabditis Genetics Center	OP50
E. coli HT115 RNAi bacteria (targeting *sma-1*)	This study	R31.1 (ORF-ID)
E. coli HT115 RNAi bacteria (targeting *frm-1*)	Source Bioscience (Ahringer library)	ZK270.2 (ORF-ID)
E. coli HT115 RNAi bacteria (targeting *unc-44*)	Source Bioscience (Ahringer library)	B0350.2 (ORF-ID)
E. coli HT115 RNAi bacteria (targeting *perm-1*)	Source Bioscience (Ahringer library)	T01H3.4 (ORF-ID)
Chemicals, peptides, and recombinant proteins		
Recombinant Cas9 protein	In-house	N/A
Prescission protease	In-house	N/A
Isopropyl b-D-1-thiogalactopyranoside (IPTG)	NZYTech	Cat#MB026
Latrunculin A	Sigma-Aldrich	Cat#L5163
FM4-64	Invitrogen	Cat#T13320
Pierce ECL Western Blotting Substrate	Thermo Fisher Scientific	Cat#32106
Nitrocellulose membrane	Amersham	Cat#GE10600001
Triton X-100	BDH Prolabo	Cat#437002A
Tween	BDH Prolabo	Cat#437082Q
Deposited data		
Code to run the simulation is available at https://gitlab.com/JulioMBelmonte/cytokinesis2021	N/A	N/A
Experimental models: Organisms/strains		
C. elegans N2 Bristol	Caenorhabditis Genetics Center (CGC)	N2
ltIs157 [pAC16;pie-1/LifeAct::GFP; unc-119 (+)]; ltIs37 [pAA64; pie-1/mCherry::his-58; unc-119 (+)]; unc-119(ed3) III (?)	Our lab	GCP21
ltIs157 [pAC16;pie-1/LifeAct::GFP; unc-119 (+)]; unc-119(ed3) III (?); prtSi2[pAC71; Pnmy-2:nmy-2reencoded::mCherrry::StrepTagII::3′UTR-nmy-2; cb-unc-119(+)]II	Our lab	GCP22
nmy-2(cp13[nmy-2::GFP+LoxP]) I; unc-119(ed3) III (?); ltIs37 [pAA64; pie-1/mCherry::his-58; unc-119 (+)]	Our lab	GCP113
plst-1(prt89) IV	Our lab	GCP564
plst-1(prt89) IV; nmy-2(cp13[nmy-2::GFP+LoxP]) I; unc-119(ed3) III (?); ltIs37 [pAA64; pie-1/mCherry::his-58; unc-119 (+)]	This study	GCP570

(*Continued on next page*)

Continued

REAGENT OR RESOURCE	SOURCE	IDENTIFIER
atn-1(prt87)V; plst-1(prt89) IV; nmy-2(cp13 [nmy-2::GFP +LoxP]) I; unc-119(ed3) III (?); ltIs37 [pAA64; pie-1/mCherry::his-58; unc-119 (+)]	This study	GCP602
plst-1(prt89) IV; ijmSi8[pJD362; Pmex-5::gfp::tbb-2; mCherry::his-11; cb-unc-119(+)] II; unc-119(ed3) III (?)	This study	GCP646
ltSi1188[pDC600; Pmex-5::GFP1-10::3′UTR-tbb-2::gpd-2/3 operon linker::mCherry-his-15::3′UTR-unc-54; cb-unc-119(+)] II; unc-119(ed3) III (this is OD4016 after 6 outcrosses)	This study	GCP794
sma-1ΔPH(prt133)V	This study	GCP808
sma-1ΔPH(prt133) V; nmy-2(cp13[nmy-2::GFP+LoxP]) I; unc-119(ed3) III (?); ltIs37 [pAA64; Ppie-1::mCherry::his-58; unc-119 (+)]	This study	GCP809
plst-1(msn190[plst-1::GFP]) IV; nmy-2(cp52 [nmy-2::mKate2+ LoxP unc-119(+) LoxP]I; ltIs37 [pAA64; pie-1/mCherry::his-58 + unc-119(+)]; unc-119(ed3) III (?)	This study	GCP831
[plst-1(msn190[plst-1::GFP])] IV; ltIs37 [pAA64; pie-1/mCherry::his-58 +unc-119(+); unc-119(ed3) III (?)	This study	GCP832
plst-1(prt89) IV; sma-1ΔPH(prt133) V; nmy-2(cp13[nmy-2::GFP +LoxP]) I; unc-119(ed3) III (?); ltIs37 [pAA64; pie-1mCherry::his-58; unc-119 (+)] IV	This study	GCP838
sma-1ΔABD#1(prt156) V	This study	GCP901
plst-1(prt89) IV; ltIs157 [pAC16; pie-1/LifeAct::GFP; unc-119 (+)]; prtSi2 [pAC71;Pnmy-2::nmy-2reencoded::mCherry::StrepTagII::3′UTR-nmy-2; cb-unc-119(+)] II; unc-119(ed3) III (?)	Our lab	GCP927
sma-1ΔSH3(prt163) V	This study	GCP986
sma-1::6xGFP11(prt159) V; ltSi1188 [pDC600; Pmex-5::GFP1-10::3′UTR-tbb-2::gpd-2/3 operon linker::mCherry-his-15::3′UTR-unc-54; cb-unc-119(+)] II; unc-119(ed3) III (?); nmy-2(cp52[nmy-2::mKate2+LoxP unc-119(+) LoxP] I	This study	GCP991
plst-1(prt89) IV; sma-1ΔSH3(prt163) V; nmy-2(cp13[nmy-2::GFP+LoxP]) I; unc-119(ed3) III (?); ltIs37 [pAA64; pie-1/mCherry::his-58; unc-119 (+)] IV	This study	GCP1014
sma-1ΔSH3(prt163) V; unc-119(ed3) III (?); nmy-2(cp13[nmy-2::GFP+LoxP]) I; ltIs37 [pAA64; pie-1/mCherry::his-58; unc-119 (+)] IV	This study	GCP1036
sma-1Δ11SR(prt192) V	This study	GCP1102
sma-1ΔABD#2(prt185) V	This study	GCP1138
ltIs157 [pAC16;pie-1/LifeAct::GFP; unc-119 (+)]; unc-119(ed3) III (?); prtSi2[pAC71; Pnmy-2:nmy-2reencoded::mCherrry::StrepTagII::3′UTR-nmy-2; cb-unc-119(+)] II; sma-1ΔSH3 (prt163) V	This study	GCP1163

(*Continued on next page*)

Continued

REAGENT OR RESOURCE	SOURCE	IDENTIFIER
plst-1(prt89) IV; ltIs157 [pAC16; pie-1/LifeAct::GFP; unc-119 (+)]; prtSi2[pAC71;Pnmy-2::nmy-2reencoded::mCherry::StrepTagII::3′UTR-nmy-2; cb-unc-119(+)] II; unc-119(ed3) III (?); sma-1ΔSH3 (prt163) V	This study	GCP1164
ltIs157 [pAC16;pie-1/LifeAct::GFP; unc-119 (+)]; unc-119(ed3) III (?); prtSi2[pAC71; Pnmy-2:nmy-2reencoded::mCherrry::StrepTagII:: 3′UTR-nmy-2; cb-unc-119(+)] II; sma-1ΔPH(prt133) V	This study	GCP1169
plst-1(prt89) IV; ltIs157 [pAC16; pie-1/LifeAct::GFP; unc-119 (+)]; prtSi2 [pAC71;Pnmy-2::nmy-2reencoded:: mCherry::StrepTagII::3′UTR-nmy-2; cb-unc-119(+)] II; unc-119(ed3) III (?); sma-1ΔPH(prt133) V	This study	GCP1170
ltIs157 [pAC16;pie-1/LifeAct::GFP; unc-119 (+)]; unc-119(ed3) III (?); prtSi2[pAC71; Pnmy-2:nmy-2reencoded::mCherrry::StrepTagII:: 3′UTR-nmy-2; cb-unc-119(+)] II; sma-1 ΔSR11(prt192)V	This study	GCP1176
plst-1(prt89) IV; ltIs157 [pAC16; pie-1/LifeAct::GFP; unc-119 (+)]; prtSi2 [pAC71;Pnmy-2::nmy-2reencoded::mCherry::StrepTagII:: 3′UTR-nmy-2; cb-unc-119(+)] II; unc-119(ed3)III (?); sma-1 ΔSR11 (prt192) V	This study	GCP1187
sma-1::splitGFP (prt159) V; ltSi1188[pDC600; Pmex-5::sGFPS1-10::tbb-2_3′UTR::gpd-2/3 operon linker::mCherry-his-15::unc-54-3′UTR; cb-unc-119(+)] II; unc-119(ed3) III (?); plst-1 [prt198(plst-1::linker::mCherry)] IV	This study	GCP1207
sma-1::splitGFP(prt159) V; ltSi1188[pDC600; Pmex-5::sGFPS1-10::tbb-2_3′UTR::gpd-2/3 operon linker::mCherry-his-15::unc-54-3′UTR; cb-unc-119(+)] II; unc-119(ed3) III (?); zbIs2 (pie-1::lifeAct::RFP)	This study	GCP1208
plst-1[prt198(plst-1::mCherry)] IV	This study	GCP1209
sma-1(ru18) V	CGC	AZ30
ijmSi8[pJD362; Pmex-5::GFP::tbb-2; mCherry::his-11; cb-unc-119(+)] II; unc-119(ed3) III	Dumont Lab	JDU21
unc-119(ed3) III; ltIs20 [pASM10; pie-1/GFP::unc-59; unc-119 (+)]	OD Lab	OD26
unc-119(ed3) III; ltIs28 [pASM14; pie-1/GFP-TEV-StrepTagII::ANI-1; unc-119 (+)]; ltIs37 [pAA64; pie-1/mCherry::his-58; unc-119 (+)]	OD Lab	OD130
ltSi1188 [pDC600; Pmex-5::GFP1-10:: 3′UTR-tbb-2::gpd-2/3 operon linker:: mCherry::his-15::3′UTR-unc-54; cb-unc-119(+)] II; unc-119(ed3) III	OD Lab	OD4016
spc-1(cas815[spc-1::GFP]) X	Ou Lab	GOU2936

(*Continued on next page*)

Continued

REAGENT OR RESOURCE	SOURCE	IDENTIFIER
unc-70(cas962[GFP::unc-70]) V	Ou Lab	GOU3103
plst-1(msn190[plst-1::GFP]) IV	Zaidel-Bar Lab	RZB213
plst-1(msn190[plst-1::gfp]) IV; zbIs2 (pie-1::LifeAct::RFP)	Zaidel-Bar Lab	RZB217
erm-1(mib15[erm-1::eGFP]) I	Boxem Lab	BOX213
Oligonucleotides		
See Table S2	N/A	N/A
Recombinant DNA		
Expression vector L4440	Bioscience/ Ahringer library	L4440
Plasmid pJA58	Fire Lab/ Addgene	CAS 59933
Plasmid pAC571	This study	pAC571
Plasmid pDC592	Cheerambathur Lab	pDC592
Plasmid pDD162	Goldstein Lab	pDD162
Expression vector for sma-1 ABD - pGEX-6P1_GST_TEV_sma-1_ABD (see STAR Methods for details)	This study	pAC543
Expression vector for sma-1 PH - pGEX-6P1_GST_TEV_sma-1_PH (see STAR Methods for details)	This study	pAC553
Software and algorithms		
ImageJ (Fiji)	Schindelin et al.[60]	https://imagej.net/software/fiji/; RRID: SCR_003070
GraphPad Prism	GraphPad Software	http://www.graphpad.com/; RRID: SCR_002798
Cytosim	Nedelec & Foethke[61]	https://gitlab.com/JulioMBelmonte/cytosim
MagicPlotPro	Magicplot Systems, LLC	https://magicplot.com
MATLAB / Particle Image Velocimetry (PIV)	MathWorks	https://openresearchsoftware.metajnl.com/articles/10.5334/jors.bl/; RRID:SCR_001622

RESOURCE AVAILABILITY

Lead contact

Further information and requests for resources and reagents should be directed to and will be fulfilled by the Lead Contact Ana X Carvalho (anacarvalho@ibmc.up.pt).

Materials availability

Key strains, plasmids and antibodies are available upon request through the Lead Contact.

Data and code availability

Data reported in this paper will be shared by the lead contact upon request.

The code necessary to run the simulations is freely available and can be found at https://gitlab.com/JulioMBelmonte/cytokinesis2021. Further information regarding the computational aspects of this work should be directed to Julio Belmonte (jbelmon2@ncsu.edu).

Any additional information required to reanalyze the data reported in this work is available from the Lead Contact upon request.

EXPERIMENTAL MODEL AND SUBJECT DETAILS

C. elegans strains

The *C. elegans* strains used in this study are listed in the Key resources table. Strains were maintained at 20°C on nematode growth medium (NGM, for 1 L: 3 g NaCl, 17 g agar, and 2.5 g peptone, plus 1 mL of 1 M $CaCl_2$, 1 mL 5 mg/mL cholesterol in ethanol, 1 mL of 1 M $MgSO_4$ and 25 mL of 1 M KH_2PO_4 pH 6 after autoclaving at 110°C for 30 minutes and cooling down to 55°C) plates seeded with *Escherichia coli* OP50.

CellPress
OPEN ACCESS

METHOD DETAILS

RNA interference

RNAi was performed either by feeding animals with *E. coli* HT115 bacteria expressing double stranded RNA (dsRNA) or by injecting animals with dsRNA.

To produce dsRNA for injection, primers with tails containing T3 and T7 RNA polymerase promoters were used to amplify the desired regions from N2 cDNA (Table S2). The PCR products were transcribed with T3 or T7 RNA polymerases (MEGAscript Transcription Kit; ThermoFischer Scientific). Transcription reactions were cleaned up (NucleoSpin RNA Clean-up, Macherey-Nagel) and diluted with 3 × soaking buffer (32.7 mM Na_2HPO_4, 16.5 mM KH_2PO_4, 6.3 mM NaCl, and 14.1 mM NH_4Cl). Injection of dsRNA at ~1 μg/μl was performed in L4-stage animals of strains GCP113 or GCP570, and the animals were incubated at 20°C for 48-54 hours prior to dissection for imaging. RNAi by injection was used to deplete ATN-1, PLST-1, FLN-1, UNC-70, UNC-59, ANI-1, and ERM-1. In the case of *fln-1(RNAi)*, dsRNAs fln-1#1 and fln-1#2 were mixed together to cover all isoforms.

For RNAi by feeding, we used the RNAi feeding vector L4440 transformed into *E. coli* HT115. L4440 vectors for RNAi of *cor-1, frm-1, unc-44 or perm-1* were obtained from the Ahringer library (Source Bioscience) and sequenced to confirm the gene target. L4440 for *sma-1* RNAi was generated by inserting a *sma-1* fragment amplified from N2 cDNA (primers 5′-CCCCCGATATCGACACCCTTT-CAAATG-3′ and 5′-CCCCCGATATCCCTTCTGTTCCATCTCGTTTC-3′) into the EcoRV restriction enzyme site. The bacteria were grown overnight at 37°C in 50 mL Luria broth medium containing 12.5 μg/ml tetracycline and 100 μg/ml ampicillin. The culture was centrifuged for 10 minutes at 2,500 *g*. The cell pellet was resuspended in 2.5 mL Luria broth medium containing 12.5 μg/ml tetracycline, 100 μg/ml ampicillin, and 1 mM IPTG. 75 μl were used to inoculate NGM plates to which 100 μl of a 1:1:1 mix of 100 mg/ml ampicillin, 1 M IPTG, and 5 mg/ml tetracycline had been added 2 hours prior. The expression of double-stranded RNA was induced overnight at room temperature and in the dark. 25-30 L4-stage animals of strains GCP22, GCP113, GCP570, GCP646, GCP927 or GCP1170 were added to the plates and incubated at 20°C for 48-54 hours prior to dissection for imaging.

Generation of mutants using CRISPR/Cas9

Guide RNAs and repair templates used to edit the *C. elegans* genome, as well as diagnostic primers used to screen for positive editing events, are listed in Table S2. Modified regions were confirmed by sequencing. To remove potential off-target mutations, modified animals were subjected to six rounds of outcrossing with wild-type N2 animals. Other modifications (e.g., fluorescent markers) were subsequently introduced by mating.

For generation of *sma-1ΔPH*, *sma-1ΔABD#1* and *atn-1ΔABD*, we used a plasmid-based approach, in which a single guide RNA (sgRNA) and the Cas9 protein are co-expressed from pDD162.[62] Guide sequences were chosen using the online tools https://zlab.bio/guide-design-resources and http://crispor.tefor.net/. Single-stranded repair templates (Integrated DNA Technologies) included 50-60 bp homology regions flanking the Cas9 cleavage site and, when necessary, silent mutations to avoid repair template recognition by Cas9. For *sma-1*ΔABD#1, the intended modification was the removal of the entire ABD. However, the last 14 residues of the CH2 were retained. The sequence of the modified region is as follows: 5′-cagGTTCGTGTTCCAACAAGTGGTGCACCACCAGT TCGCGCAGATGCCAATGGAACAGATCAAGACGAGTTCAATAATGAGACACTGTACTTTGAAAGATCACGCATTCGGACATCAATCA TTACATATGTTTCCTTGTACTATCATCATTTTGCAAAGCAAAAGACTGAGATGACAGGAGCTCGACGTATTGCTAATgtaagtgttta-taagttcatg-3′ (bases in lowercase indicate intron regions).

For *sma-1ΔSH3, sma-1ΔABD#2*, and *sma-1Δ11SR*, we injected a ribonucleoprotein (RNP) mix consisting of crRNA/tracrRNA (CRISPR/Cas9 design tool ht https://www.idtdna.com/site/order/designtool/index/CRISPR_PREDESIGN; Integrated DNA Technologies) and purified recombinant Cas9 protein. The repair template for *sma-1ΔABD#2* was partially single-stranded (assembled by overlap extension PCR[63]) and consisted of 120-bp homology regions flanking the Cas9 cleavage site, silent mutations to avoid repair template recognition by Cas9, and the *sma-1* intron between exons 3 and 4. For *sma-1ΔSH3* and *sma-1Δ11SR*, the single-stranded repair template included 50-bp homology regions flanking the Cas9 cleavage site. For *sma-1ΔABD#2*, the intended modification was the removal of the CH1 domain (part of exon 3 and exon 4) leaving the intron between exons 3 and 4 but not the intron between exons 4 and 5. However, sequencing of the modified region revealed that the first 17 residues of CH1 were retained (retains part of exon 3, entire intron between exons 3 and 4, and part of exon 5): 5′-aaagttttaaagatccgaaaaaaaactgagaacgtttagaaatatttaacagttcaattagcat-caagttcataatgatttttttcagGTTCGTGTTCCAACAAGTGGTGCACCACCAGTTCGCGCAGATGCCAATGGAACAGATCAAGACGAGTTCA ATAATGAGACACTGTACTTTGAAAGATCACGCATTCGGACACTGCAGGACGAACGTGTGCACATTCAGAAGAAGACGTTCACAAAA TGGTGCAACTCCTTTCTTAATCGG- intron3/4 as in sma-1 transcript R31.1a, Wormbase version WS279 - GATGAGGAAGAGCGTG GAGAGCGAAAACATGCCAAAGATGCCTTGCTGTTGTGGTGTCAGAGAAAAACAGCTGGATATCCAAATGTTCGCATCGAAAACTTC ACTACAAGTTGG-3′. For *sma-1Δ11SR* the intended modification was the removal of 13 spectrin-repeats, however only 11 spectrin repeats were removed (mid spectrin repeat #14 to mid spectrin repeat #25). The obtained sequence is as follows: 5′-CGTGACGTT GACGAGTTTGAGCAATGGATGGCAGACAAAATGGCCAACATGCCACG*CTCACACGAACTGT*ACGAGATTGATCGCTTGAAGAAG CGTGCGGATGGACTTCTAGCCAGAGAGCATCACGATGCAATGTCGATTGCTGCGAAACAACGCAAACTGGAAGCATTGTTCGGA GACCTCTGCAGAGAATGTGCCAGACGACGAACTCAAATTGTTGATGCTTCCAAATATCACAAGTTTGTTAGACAAGCCGATGATTT GTCAGACTGGCTACGTGAGAAAGAAAGGTCCGCATCAGCTGAGGATTACGGTCAAGATTTGGAGGATTGCCAACAAATTATTGAG CAGTTCGAATCTACAGTTCGTGAATTGGCAGCTGCTGGAGAGCGTGTTGCTGCTGTCCAACGTGCACAAGAAGATCTTCTACGAA GTGGACATCCATATGGAGCATCAATCACTGCAAAAGGCGCTGATGTTCAGAGACTATGGACTCATGTCAATGAAGTGGCTAATGA GAGAAAGCAAGCGTTGAATGGAGCTCGTCAAGTTCATCGATTCGACCAAGAAGCCGATCAGATATTGAATTGGTTACAAGATAAGG

AAGCGACTGGAGTAGCAATGGAACAGGAAGATCTTTCGAGAGCTGATCTTGCTTCCGTGAA-3′ (14 base pairs in italics replaced the region removed from mid spectrin repeat #14 to mid spectrin repeat #25, and did not cause a frameshift).

In all cases repair templates and pDD162 or RNPs were injected into gonads of young adult N2 hermaphrodites. To facilitate the identification of successfully injected animals, injection mixes also contained a repair template and pJA58 (a gift from Andrew Fire, Addgene plasmid # 59933; http://addgene.org/59933; RRID: Addgene_59933) or crRNA to generate the R92C mutation in *dpy-10*, which causes a dominant roller phenotype in mutated F1 progeny.[64]

Tagging of endogenous SMA-1 and PLST-1

Guide RNAs and repair templates used, as well as diagnostic primers used to screen for positive editing events, are listed in Table S2. All modified regions were confirmed by sequencing.

To generate an endogenous fluorescent version of SMA-1, we used the self-complementing split GFP system.[33] We inserted 6 copies of GFP11 in tandem downstream of the *sma-1* open reading frame using plasmid-based CRISPR/Cas9-mediated genome editing, as described above. The plasmid template used for homology recombination was pAC571, which was built using Gibson assembly.[65] The fragments used for pAC571 assembly were as follows: pBluescript backbone, amplified with primers 5′-CATGTGAGCAAAAGGCCAGC-3′ and 5′-ATCGCCCTTCCCAACAGTTG-3′; 1 kb left homology region in the *sma-1* open reading frame, amplified from N2 genomic DNA (gDNA) with primers 5′-TCAGGCTGCGCAACTGTTGGGAAGGGCGATAGCTTTCTTCCCTCCGTC-3′ and 5′ CTTTGAATGTTTGGATCCACG**T**TT**A**AA**C**AA**G**GATCCGAATCCTTTTCGTTCTG-3′ (bases in bold indicate silent mutations introduced to avoid repair template recognition by Cas9); 6xGFP11, amplified from pDC592 with primers 5′-**C**TT**G**TT**T**AA**A**CGTGGATCCAAACATTCAAAG*GGAGGGAGGGCCGGCTCTG*-3′ and 5′-GGTGATTCCAGCAGCGTTAACGTACTCAT-3′ (bases in bold indicate silent mutations introduced to avoid repair template recognition by Cas9; bases in italics indicate part of the linker region); and 1 kb right homology region in the *sma-1* 3′UTR, amplified from N2 gDNA with primers 5′-ATGAGTACGTTAACGCTGCTGGAATCACCTAAATAC**G**TCACCACACGCTGATCTTC-3′ and 5′-CTGGCCTTTTGCTGGCCTTTTGCTCACATGCCATTTTGTTGGATTGCTC-3′ (bases in bold indicate silent mutations introduced to avoid repair template recognition by Cas9). Animals expressing SMA-1::6xGFP11 were crossed with animals expressing GFP1-10 from the *mex-5* promoter (GCP794 strain). GCP794 was obtained by subjecting the strain OD4016 (kindly provided by Arshad Desai) to six rounds of outcrossing with N2 animals.

To generate an endogenous mCherry-tagged version of PLST-1 (PLST-1::mCherry), we generated a partially single-stranded repair template (hybrid template), as in Dokshin et al., 2018.[63] The repair template consisted of 120-145-bp homology regions flanking the Cas9 cleavage site, silent mutations to avoid repair template recognition by Cas9, and a 10 amino acid linker followed by the mCherry tag. The long fragment of the repair template was amplified with the primers: 5′ aaaatcgtccaaaaccccaaattgttttcagGTGAAGCCAAAAATGGTGTTGACAGTGTTTGCATGTCTAATGGCTCGTGACTATCTTCCCGATATGAAGCAAGGAGCAGCTTCTGCTCC**G**AT**C**GT**C**CC**A**ATGAT**C**AATGGAAAT*GAGGACCCTTGGAGGGTACCGGTAGAAAAA*ATGGTCTCAAAGGGTGAAGAAGATA-3′ (145 bp of homology region in the *plst-1* open reading frame; bases in bold indicate silent mutations introduced to avoid repair template recognition by Cas9; bases in italics correspond to the 10 amino acid linker, bases in lowercase indicate introns) and 5′ aatttttgtgagaaaaaagatggaaaaacgggaaaatagagatatatatatggaggaaaatttgtatttccgcgatttttttcggcgggaaattcaagaaattcgaaatttttgcagaaCTACTTATACAATTCATCCATGCCACC-3′ (120 bp of homology region in the *plst-1* 3′ UTR; underlined bases in lowercase indicate 3′UTR region). The short fragment of the repair template was amplified with the following primers: 5′ **G**AT**C**GT**C**CC**A**ATGATC**A**ATGGAAAT*GAGGACCCTTGGAGGGTACCGGTAGAAAAA*ATGGTCTCAAAGGGTGAAGAAGATA-3′ (bases in bold indicate silent mutations introduced to avoid repair template recognition by Cas9; bases in italic indicate the 10 amino acid linker) and 5′ CTACTTATACAATTCATCCATGCCACC-3′. Animals expressing PLST-1::mCherry were subjected to six rounds of outcrossing with N2 animals.

Live imaging

Gravid hermaphrodites were dissected and one-cell embryos were mounted in a drop of M9 (86 mM NaCl, 42 mM Na_2HPO_4, 22 mM KH_2PO_4 and 1 mM $MgSO_4$) on 2% agarose pads overlaid with a coverslip. Live imaging was performed at 20°C.

Images in Figures 1, 3D, 4, 5, 6, 7, S1B, S1E, and S3–S6 were acquired on a spinning disk confocal system (Andor Revolution XD Confocal System; Andor Technology) with a confocal scanner unit (CSU-X1; Yokogawa Electric Corporation) mounted on an inverted microscope (Ti-E, Nikon) equipped with a 60x oil-immersion Plan-Apochromat objective (N.A. 1.4), extra 1.5x magnification, and solid-state lasers of 488 nm (50 mW) and 561 nm (50 mW). For image acquisition, an electron multiplication back-thinned charge coupled device camera (iXon Ultra 897; Andor Technology) was used. Acquisition parameters, shutters and focus were controlled by Andor iQ3 software. Images in Figures 3 and S7A were acquired on a similar system equipped with a confocal scanner unit (CSU-22; Yokogawa Electric Corporation), an iXon EM+ DU-897 (Andor Technology), mounted on an inverted microscope (IX81; Olympus) equipped with a 100x oil-immersion UPLSAPO objective (N.A. 1.4), extra 2x magnification, and solid-state lasers of 488 nm (50 mW) and 561 nm (50 mW).

For cortical imaging, 7 × 0.5 μm z stacks were collected every 5 s in embryos of strains GCP21, GCP22, GCP113, GCP570, GCP809, GCP831, GCP832, GCP838, GCP927, GCP991, GCP1014, GCP1036, GCP1163, GCP1164, GCP1169, GCP1170, GCP1176, GCP1187, GCP1207, GCP1208, RZB217, OD26, OD130 and GOU2936 (Figures 1A, 3, 4E, 5A, 5B, 6A, 6B, 6D, 6E, 7J, S5A, S6, and S7A). An image at the center of the embryo was also acquired to determine the timing of anaphase onset. For central plane imaging in Figures 1A, 2C, 5D, S1B, S1F, and S3A, 6 × 1 μm z stacks were collected every 10 s in embryos of strains GCP21, GCP22, GCP113, GCP570, GCP646, GCP831, GCP832, GCP927, GCP991, OD26, OD130 and GOU3103. For fluorescence

recovery after photobleaching (FRAP) experiments (Figures 6F–6H and S6), a FRAPPA photobleaching module (Andor Technology) placed between the spinning disk head and the microscope was used. Photobleaching was performed by 3 sweeps of a 405 nm laser with 100% power and 40 μs dwell time.

For measurement of total cytokinesis time, contractile ring diameter decrease, ring constriction rate and percentage of cytokinesis completion/failure in Figures 1C, 1D, 2A, 2D, 4C, 4D, 7I, and S2D, images were acquired with an epifluorescence microscope (Zeiss Axio Observer Z1) equipped with a 63x Plan-Apochromat objective (N.A. 1.4), a Colibri.2 LED light source, and an Orca Flash 4.0 camera (Hamamatsu). Acquisition parameters, shutters, and focus were controlled by Zen 2.3 software (Zeiss). 7 × 1 μm z stacks were collected every 10 s in embryos of strains GCP113, GCP570, GCP809, GCP838, GCP1014 and GCP1036.

Image processing

Image processing and analysis was performed using Fiji (ImageJ; National Institutes of Health) or MATLAB (MathWorks). Z stacks taken on the cell cortex were projected using the maximum intensity projection tool. The equatorial region of the central plane was selected to make the kymographs displayed in Figures 2C and S1F, the equatorial region of the maximum projection of cortical planes was selected to make the kymographs displayed in Figures 5B, 6B, and S5A, and a 150 × 5 pixel rectangle positioned at the center of cortical plane was selected to make the kymographs in Figure S4D, using the Make Montage tool. Images in each figure panel are scaled equally, except for Figures 1A and 3. Graph plotting, curve fitting and linear regressions were performed with Prism 8.0 (GraphPad Software) or MagicPlotPro 2.8.2.

Latrunculin A treatment

Acute treatment with Latrunculin A in Figures 6D–6H and S6 was performed in *perm-1(RNAi)* permeabilized embryos.[41] 25–30 L4 animals were placed on a plate containing 0.005 mM isopropyl β-d-1-thiogalactopyranoside (IPTG) and *E. coli* HT115 bacteria expressing dsRNA against *perm-1*. After incubation for 14–18 hours at 20°C, adult hermaphrodites of strains GCP22 or GCP113 were dissected and permeabilized embryos were filmed in meiosis medium (25 mM HEPES, pH 7.4, 0.5 mg/ml inulin, 20% heat-inactivated fetal bovine serum, and 60% Leibowitz-15 medium) without compression. 10 μM Latrunculin A (Sigma) was added at anaphase onset. At the end of each video, medium containing 33 μM FM4-64 (Molecular Probes) was added to the imaging chamber to confirm that the imaged embryo was permeable.

Generation of antibodies against SMA-1

Two affinity-purified rabbit polyclonal antibodies against the actin-binding domain (SMA-1 ABD in Figures 4B and S1A) and pleckstrin homology domain (SMA-1 PH in Figures S2B and S2C) of SMA-1 were generated.To produce GST-tagged ABD, cDNA encoding amino acid residues 195-519 of SMA-1 (residue numbers as in isoform a, from transcript R31.1a, Wormbase version WS279) was cloned into the EcoRI and NotI restriction sites of pGEX-6P1 using primers 5′-CCCGAATTCATTTCCGGAGACAAACTCGG-3′ and 5′-CCCGCGGCCGCTTCCTGTCTTTGAAGCTCGGC. To produce GST-tagged PH domain, cDNA encoding residues 3689-3898 of SMA-1 was cloned into the BamHI and NotI restriction sites of pGEX-6P1 using primers 5′-CCCGGATCCAGAAAGACTCAG-GAAATCTCTC-3′ and 5′-CCCGCGGCCGCTTAGTTGTACGCATACGACTTGAG-3′. GST::ABD and GST::PH were expressed in *E. coli* BL21 and Rosetta, respectively, purified and injected into rabbits at the in-house Animal Facility. Sera were affinity purified on a HiTrap N-hydroxysuccinimide column (GE Healthcare) against covalently coupled ABD and PH (TEV-cleaved with prescission protease in cleavage buffer: 50 mM HEPES pH 7.6, 150 mM NaCl, 1 mM EDTA, 1 mM DTT, 0.01% Tween 20, at 4°C overnight), aliquoted in 10% glycerol, snap-frozen and stored at −80°C.

Protein extracts and immunoblotting

For the immunoblots in Figures 4B, S1A, S2B, and S2C, protein extracts were prepared from 100 adult stage animals of strains N2, GCP808, AZ30, GCP986 and GCP564. Animals were collected in M9 medium with 0.1% Triton X-100 and washed three times in the same medium. The pellet of worms was resuspended in 100 μl of SDS-PAGE sample buffer (250 mM Tris pH 6.8, 30% v/v glycerol, 8% w/v SDS, 200 mM DTT and 0.04% w/v bromophenol blue) and one-third of the volume of quartz sand (Sigma) was added. Tubes were subject to three 5-minute cycles of boiling at 95°C and vortexing, after which the quartz sand was pelleted and the supernatant recovered. Protein samples (20-30 μl, equivalent to 20-30 animals) were resolved by SDS-PAGE (8% acrylamide gel) and transferred to a 0.2-μm nitrocellulose membrane (GE Healthcare). Membranes were blocked with 5% non-fat dry milk in TBST (20 mM Tris, 140 mM NaCl, and 0.1% Tween, pH 7.6) and probed at 4°C overnight with 1 μg/ml anti-SMA-1 ABD antibody or 1 μg/ml anti-SMA-1 PH antibody and 1:5000 anti-α-tubulin antibody (DM1-α, Sigma). Membranes were washed three times with TBST, incubated with HRP-conjugated secondary antibodies (mouse anti-rabbit 1:5000 or goat anti-mouse 1:5000; Jackson ImmunoResearch) for 1 hour at room temperature, and washed again three times with TBST. Proteins were visualized by chemiluminescence using Pierce ECL Western Blotting Substrate (Thermo Fisher Scientific) and imaged in a ChemiDoc XRS+ System with Image Lab Software (Bio-Rad).

Immunofluorescence

For the immunofluorescence in Figure 3D, twelve gravid adult hermaphrodites were dissected in 5 μl of M9 buffer on a poly-L-lysine coated slide. A 13 mm^2 round coverslip was placed over the M9, and slides were placed into a container with liquid nitrogen. After flicking away the coverslip, samples were fixed for 20 minutes in −20°C methanol. Samples were re-hydrated in PBS (137 mM NaCl,

2.7 mM KCl, 8.1 mM Na_2HPO_4, 1.47 mM KH_2PO_4), twice for 5 minutes, blocked with AbDil (PBS, 2% BSA, 0.1% Triton X-100) in a humid chamber for 30 minutes at room temperature, and incubated in AbDil with rabbit anti-SMA-1 PH antibody (1:1000) and anti-α-tubulin antibody (1:1000, DM1-α, Sigma), overnight at 4°C. After washing four times for 5 minutes in PBS, samples were incubated in AbDil with Alexa Fluor 488 anti-rabbit IgG (1:300; Jackson ImmunoResearch) and Alexa Fluor 594 goat anti-mouse IgG (1:300; Jackson ImmunoResearch) for 1 hour at room temperature. Samples were washed four times for 5 minutes in PBS and mounted in Prolong Gold (Invitrogen).

Computational simulations

We simulated the formation of cytokinetic rings using the Open Source engine Cytosim, which is capable of simulating the thermal environment of the cell as well as the forces generated by the interaction of biological fibers and binding proteins. We identified 4 essential components to simulate the assembly and maintenance of ring structures: F-actin, myosin motor minifilaments, and the crosslinkers plastin and βH-spectrin. Parameters that characterize each component are listed below (corresponding references are in Table S3).

Actin fibers were modeled as a series of geometrically polarized rigid segments connected by flexible hinges, with an overall rigidity 0.075 pN μm^2. Initially segments were 0.1 μm long forming a nongrowing fiber of total length 1 μm, with a barbed and a pointed end. Actin dynamics are very complex and mostly mediated by auxiliary proteins such as formin, ADF/cofilin, capping proteins, and breakage events. We chose to model actin dynamics in simple terms, where each end of a fiber can stochastically switch between a growth state and a shrink state at fixed rates, and ends grow and shrink with pre-defined speeds. We prevented fibers from disappearing by defining a minimum length of 0.01 μm where they remain inactive until a rescue event. When the depolymerizing end encounters a crosslinker, it has a 90% chance of continuing depolymerizing (and unbinding the crosslinker) and a 10% chance of stopping depolymerizing. Values were adjusted so that average fiber length remains roughly constant.

The contraction of actin fibers into a ring is driven by molecular motors designed to model non-muscle myosin II. The backbone of the motor is a 0.15 μm long rigid solid. There are 4 binding heads on each end, equally spaced by 0.015 μm starting from the ends of the solid for a total of 8 binding domains. Each head can bind to any actin fiber within a range of 0.01 μm at a rate of 10 Hz and while bound can unbind at a rate of 0.3 Hz. While bound to an actin fiber, heads walk toward the barbed end of the fiber with a specified maximum speed which can be suppressed by the amount of drag force on the motor with a stall force of 4 pN. Maximum speed was chosen to match the proper time frame measured experimentally. Binding heads follow normal unbinding rules when reaching the end of fibers as opposed to immediately falling off. If the barbed end of an actin fiber attempts to grow or shrink while a motor head is attached, the motor head will remain attached to the end. Allowing for immediate myosin unbinding from depolymerizing barbed ends does not affect timing and success rate when all components are present, but slows down ring formation for all perturbed cases and leads to expulsion of most actin filaments from the ring midline (Figure S7D).

Plastin is a crosslinker consisting of two binding heads connected by a 0.012 μm long spring[12] with stiffness 250 pN/μm. If both heads are unbound then either head can bind any actin fiber within 0.01 μm at a binding rate of 10 Hz. While one head is bound, the second head can only bind actin segments closely aligned with the first segment. The maximum allowed angular difference between actin segments is 10 degrees. Bound heads unbind at a rate of 0.05 Hz. While attached to dynamic fibers, binding heads have a 10% chance of rescuing a depolymerizing fiber.

βH-spectrin has two heads like plastin but has an extended flexible body of 0.25 μm and no angular restriction while binding actin fibers. The backbone is modeled as a series of rigid segments of 0.05 μm in length, and a rigidity 3 orders of magnitude lower than that of our actin filaments ($7.5*10^{-5}$ pN μm^2). At each end of the βH-spectrin fiber there is a binding head with identical binding range, binding rates and rescue behavior as plastin.

We modeled cytokinetic ring assembly similarly to the work of Bidone et al.[66] We randomly placed all 4 components in a 10 μm by 4 μm rectangular space with periodic boundary conditions along the top and bottom edges. Increasing the ''circumference'' of our space by values higher than 4 μm did not change our results (Figure S7C). The initial horizontal range of our components is about 3 μm since we are concerned with the assembly of the ring itself and not the flux of material from the sides. Our space had background viscosity and temperature typical to those in cells of *C. elegans* embryos.

To quantify ring formation timing and success rate we created a metric *M* measuring the spatial distribution of myosin motors. This metric is defined by three calculations. We first created separate histograms of the horizontal and vertical positions of the center of masses of the motors. The exact binning method was unimportant, but the horizontal center bin should coincide with the ring midline since an ideal ring will concentrate all motors' horizontal position in the exact center. We then found the standard deviation of the bin counts in each direction and normalized by dividing by the largest possible deviation, representing a distribution with all motors in one bin. Since a ring should be localized in the horizontal but uniform in the vertical, we defined our metric as:

$$M = \underline{\sigma_x} * \left(1 - \underline{\sigma_y}\right) \quad \text{(Equation 1)}$$

M ranges from 0 to 1 (Figure S7B). By comparing our metric to videos of simulations, we determined that a ring had successfully assembled if *M* exceeded a threshold value of 0.5.

To reproduce experimental results, we simulated four different configurations of components. All configurations had actin fibers and myosin motors since those are the minimal components necessary to have a contractile network. We then simulated 100 trials

with (1) no crosslinkers, (2) plastin only, (3) βH-spectrin only, and (4) both plastin and βH-spectrin. We determined a final ring success rate by the percentage of successful trials ($M > 0.5$).

QUANTIFICATION AND STATISTICAL ANALYSIS

Image quantifications

The total cytokinesis time in Figure 1 was obtained by determining the time elapsed between anaphase onset and the contractile ring reaching a diameter of 5 μm, measured in the z-plane with the widest gap between the two tips of the ingressing cleavage furrow. Anaphase onset was defined by direct visualization of DNA, labeled with H2B::mCherry. Ring constriction rate was the slope of the linear region between ~75% and 10% furrow ingression.

To quantify the number of actin clusters and myosin puncta on the equatorial cortex in Figure 6C, an intensity threshold was applied (1500 gray values for NMY-2::mCherry and 2500 gray values for LifeAct::GFP) and myosin structures larger than 0.4 μm and with a circularity of 0.5-1 and actin structures larger than 0.3 μm and circularity of 0.3-1 were selected using the Analyze Particles tool (Fiji).

The percentage of cytokinesis success/failure in Figures 1C, 2A, 4C, 4D, 7I, and S2D was assessed by counting the number of one-cell embryos in which furrowing completed/did not complete and dividing it by the total number of embryos filmed.

Deviation of F-actin bundles from vertical alignment at the equatorial cortex in Figure 5C was quantified in maximum projections of cortical planes in embryos expressing LifeAct::GFP (strains GCP22 and GCP927). The Directionality plugin for ImageJ was used in a 30 × 70 pixel box placed over the furrow region, using the local gradient orientation method. The average directionality (in degrees) was determined for each time point and the deviation from vertical alignment (in degrees) was calculated by subtracting the value of the obtained angles from 90°. Absolute numbers were plotted.

Spindle behavior in Figure S3B was determined by recording the distances between the plasma membrane and the anterior/posterior centrosomes, as well as between the two centrosomes over time after anaphase onset. All curves were aligned to the center of the centrosome-centrosome distance. Values were normalized to the length of the embryo at metaphase, which was the distance between the outermost points of the embryo along the anterior-posterior axis at metaphase.

Actin cortical flows

Actin cortical flows were determined in maximum projections of cortical planes in embryos expressing LifeAct::GFP [strains GCP22 and GCP927 with and without *sma-1(RNAi)*]. Flows were analyzed between anaphase onset and the end of cytokinetic furrow ingression. Magnitude and direction of cortical flows were quantified using a Particle Image Velocimetry (PIV) MATLAB script (see Key resources table). A 216 × 128 pixel (38.5 × 22.8 μm) region was applied to all embryos to exclude cortical curved peripheries. Two iterations were performed to calculate maximum particle displacement: a larger interrogation window of 64 × 64 pixels was used in the first iteration and a smaller interrogation window of 32 × 32 pixels was used in the second iteration. Consecutive interrogation windows overlapped by 50%. After flow field generation, the 216 × 128 pixel region was divided in two adjacent anterior and posterior regions: anterior cortex (1st-148th pixel; 0.0–26.3 μm) and posterior cortex (149th-216th pixel; 26.3–38.4 μm). Each velocity vector was resolved into a Vx component along the anterior-posterior axis and a Vy component along the dorsal-ventral axis. The mean Vx and Vy in the anterior and posterior cortex were estimated for each time point and plotted as a function of time to trace the cortical flow profiles in Figure S4.

FRAP

Quantification of NMY-2::GFP fluorescence signal in FRAP experiments in Figure 6F was performed in three different regions of interest (ROIs): ROI 1 – 10 × 13 pixel box in Figure S6A or 30 × 140 pixel box in Figure S6B, corresponding to the bleached region; ROI 2 - 300 × 200 pixel oval that covers most of the cortex and is used to correct for overall photobleaching of the sample resulting from acquisition and photobleaching sweeps; and ROI 3 – 20 × 20 pixel box, corresponding to the camera background measured outside the embryo. Mean fluorescence intensity in the three ROIs was determined over time, pre- and post-photobleaching. After background subtraction and photobleaching correction, the myosin signal in the photobleached region was normalized to the average signal in that region before photobleaching and plotted over time. Curve fitting with a one-phase association exponential equation was performed to extrapolate the half time of recovery and mobile faction, using Prism 8.0 (GraphPad Software):

$$y = y_0 + (\text{Plateau} - y_0) \cdot \left(1 - e^{(-K*x)}\right),$$

where y0 is the fluorescence intensity right after photobleaching, Plateau is the fluorescence at infinite times, and K is the rate constant. The values of Plateau and K were obtained after fitting the curves with observed data to one phase association equation.

The half time of recovery was the time when the fluorescence intensity (y) equaled:

$$y = ((\text{Plateau} - y0) / 2) + y0$$

The mobile fraction, X_m, was calculated using the formula:

$$X_m = (\text{plateau} - y_0)/(\text{ybleached} - y_0),$$

where ybleached denotes the average fluorescence intensity of 3 time points before photobleaching.

STATISTICAL ANALYSIS

Statistical analysis was performed with Prism 8.0 software (GraphPad). Error bars represent 95% confidence interval of the SEM (95% CI), SEM (Figures 6C, S4B, and S4C), or SD (Figures 7F, 7G, and S7C). Statistical significance tests were performed using one-way ANOVA followed by Dunnett or Bonferroni's multiple comparison test, as indicated in the figure legends.

Current Biology, Volume *31*

Supplemental Information

Plastin and spectrin cooperate to stabilize the actomyosin cortex during cytokinesis

Ana Filipa Sobral, Fung-Yi Chan, Michael J. Norman, Daniel S. Osório, Ana Beatriz Dias, Vanessa Ferreira, Daniel J. Barbosa, Dhanya Cheerambathur, Reto Gassmann, Julio Monti Belmonte, and Ana Xavier Carvalho

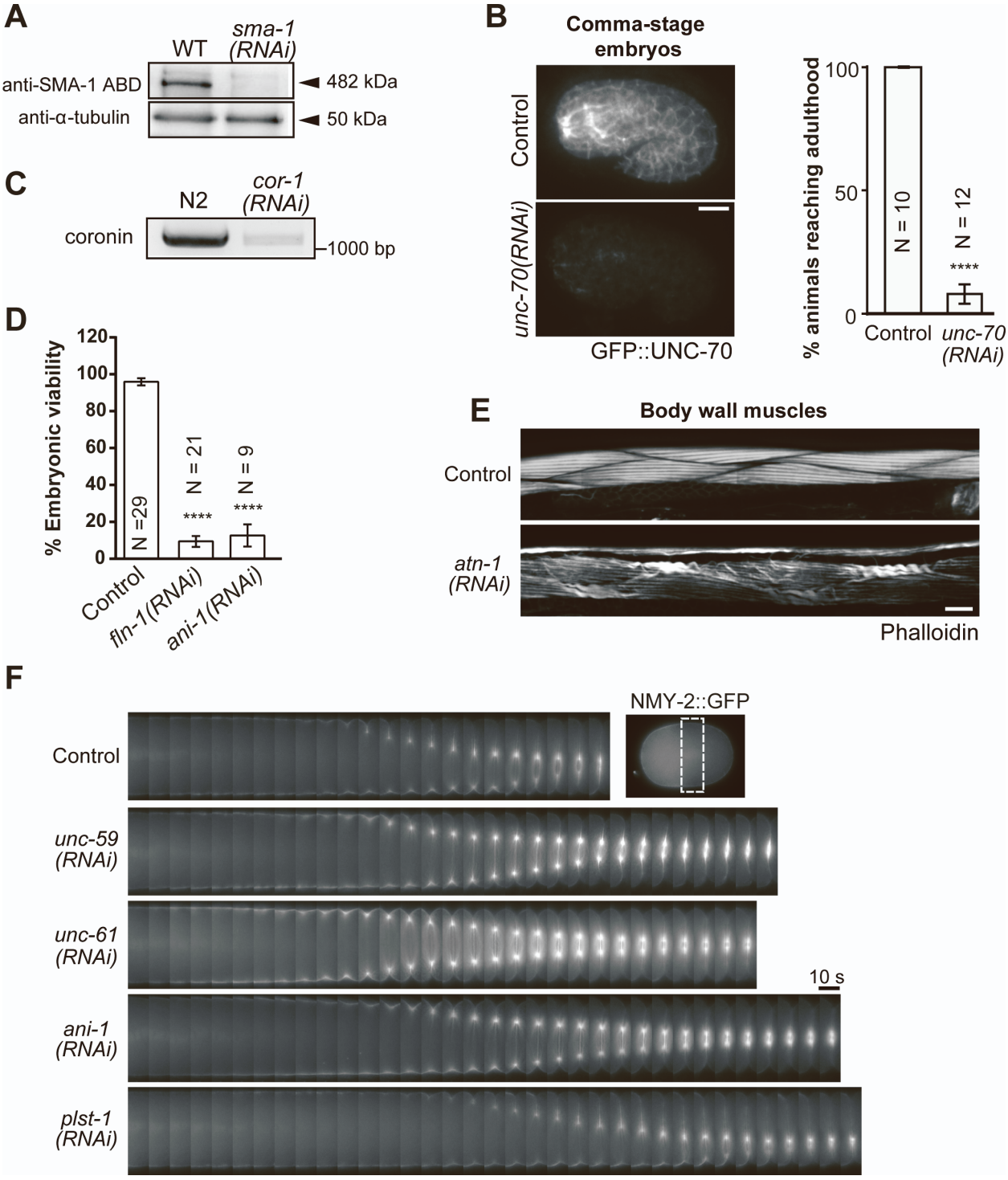
A
WT
sma-1 (RNAi)
anti-SMA-1 ABD
482 kDa
anti-α-tubulin
50 kDa
B
Comma-stage embryos
Control
unc-70(RNAi)
GFP::UNC-70
% animals reaching adulthood
100
50
0
N = 10
N = 12
****
Control
unc-70 (RNAi)
C
N2
cor-1 (RNAi)
coronin
1000 bp
D
% Embryonic viability
120
100
80
60
40
20
0
N =29
N = 21
N = 9
****
****
Control
fln-1(RNAi)
ani-1(RNAi)
E
Body wall muscles
Control
atn-1 (RNAi)
Phalloidin
F
NMY-2::GFP
Control
unc-59 (RNAi)
unc-61 (RNAi)
10 s
ani-1 (RNAi)
plst-1 (RNAi)

Figure S1. Validation of RNAi efficiency. Related to Figure 1.

(A) Immunoblot of adult *C. elegans* lysate with an antibody raised against the actin-binding domain (ABD) of SMA-1, showing efficient depletion of SMA-1 after *sma-1(RNAi)*. WT is wild-type. α-tubulin serves as the loading control. **(B)** *(left)* Stills of comma-stage embryos expressing endogenous UNC-70::GFP before and after *unc-70(RNAi)*. Scale bar, 10 μm. *(right)* Percentage (mean ± 95% CI) of *unc-70(RNAi)* animals that develop to adulthood. Most *unc-70(RNAi)* animals arrest at the L1 stage, consistent with a previous study [S1]. Statistical significance was determined using unpaired two-tailed Student t-test: $^{****}p \leq 0.0001$. **(C)** RT-PCR for *cor-1* in N2 controls and after *cor-1(RNAi)* using primers Fw 5'-CGTCGACAAGGACTATCCA-3' and Rv 5'-GGAGCCAAAGTGCTCAAA-3' that amplify the 3 isoforms. Method was described previously [S2]. **(D)** Percentage of embryonic viability (mean ± 95% CI) in N2 controls, after *fln-1(RNAi)*, and *ani-1(RNAi)*, consistent with previous studies [S3,S4]. Statistical significance was determined using one-way ANOVA followed by Dunnett's multiple comparison test: $^{****}p \leq 0.0001$. **(E)** Images of body wall muscles stained with phalloidin. *atn-1(RNAi)* results in curled F-actin fibers, as expected from previous study [S5]. Method was described previously [S6]. Scale bar, 10 µm. **(F)** Images of the equatorial region in dividing one-cell embryos expressing NMY-2::GFP. The first frame corresponds to anaphase onset. Symmetric furrow closure confirms efficient RNAi-mediated depletion of UNC-59, UNC-61 and ANI-1, as described previously [S7]. Prolonged cytokinesis confirms efficient RNAi-mediated depletion of PLST-1. Scale bar, 10 μm.

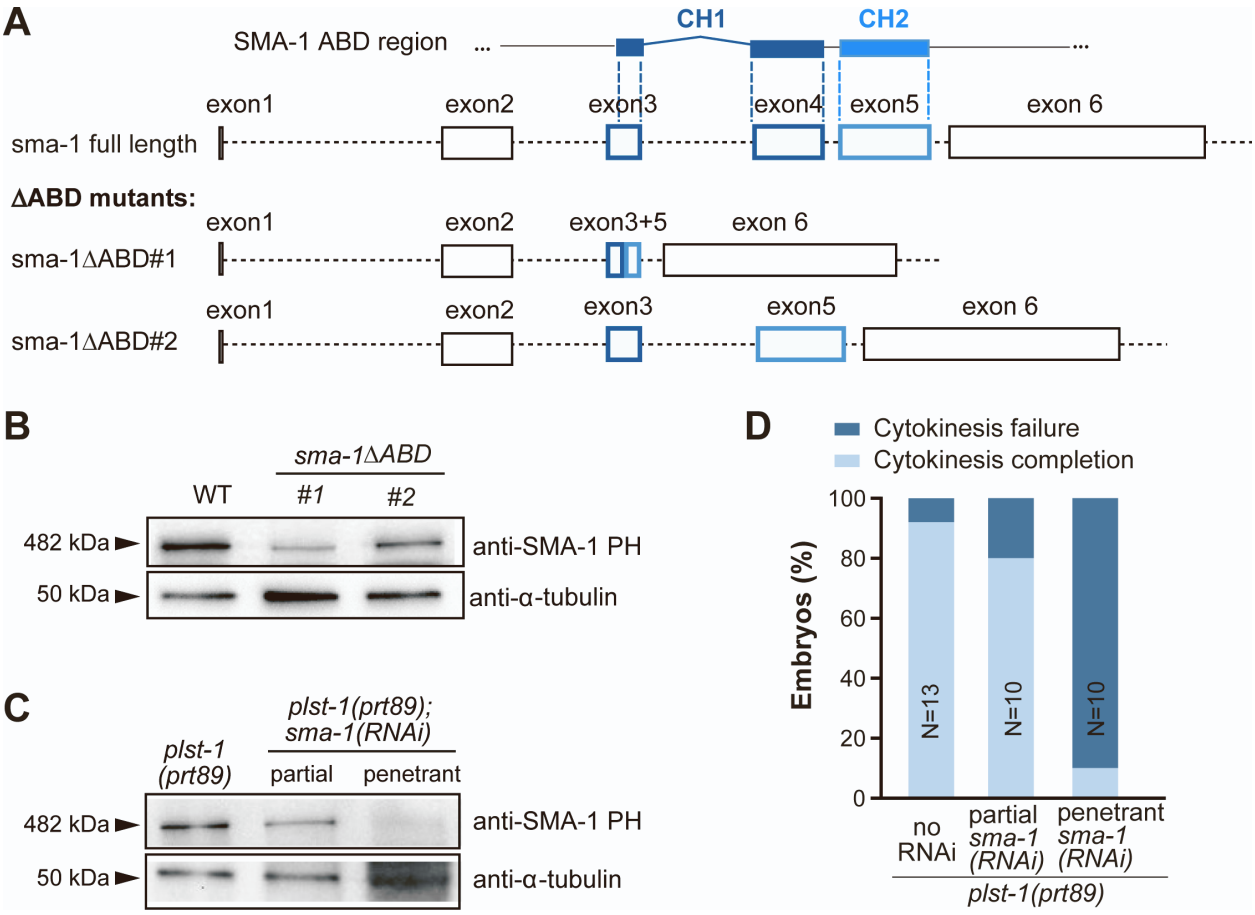
A
SMA-1 ABD region
CH1
CH2
exon1
exon2
exon3
exon4
exon5
exon 6
sma-1 full length
ΔABD mutants:
exon3+5
sma-1ΔABD#1
sma-1ΔABD#2
B
sma-1ΔABD
WT
#1
#2
482 kDa
50 kDa
anti-SMA-1 PH
anti-α-tubulin
C
plst-1(prt89); sma-1(RNAi)
plst-1 (prt89)
partial
penetrant
D
Cytokinesis failure
Cytokinesis completion
Embryos (%)
N=13
N=10
N=10
no RNAi
partial sma-1 (RNAi)
penetrant sma-1 (RNAi)
plst-1(prt89)

Figure S2. SMA-1 deletion mutants that lack most of the actin binding domain are expressed at lower levels but this is unlikely to explain the cytokinesis failure in the *plst-1(prt89)* background. Related to Figure 4.

(A) Schematic of the first 6 exons and 5 introns of the *sma-1* gene in wild-type and after editing to obtain ABD deletions (ΔABD). Part of exon 3 and exon 4 encode the first CH domain (CH1), and exon 5 encodes the second CH domain (CH2). SMA-1ΔABD#1 lacks most of exon 3, the entire exon 4, and most of exon 5. SMA-1ΔABD#2 lacks exon 4. **(B)** Immunoblot of adult *C. elegans* lysate with an affinity-purified anti-SMA-1 antibody raised against the PH domain, showing SMA-1 levels in animals expressing the two different SMA-1ΔABD versions. α-tubulin serves as the loading control. **(C)** Anti-SMA-1 immunoblot of adult *C. elegans* lysate, showing protein levels in *plst-1(prt89)* animals after partial or penetrant *sma-1(RNAi)*. α-tubulin serves as the loading control. (**D**) Percentage of cytokinesis completion/failure in one-cell *plst-1(prt89)* embryos after partial and penetrant depletion of SMA-1. N indicates the number of embryos analyzed.

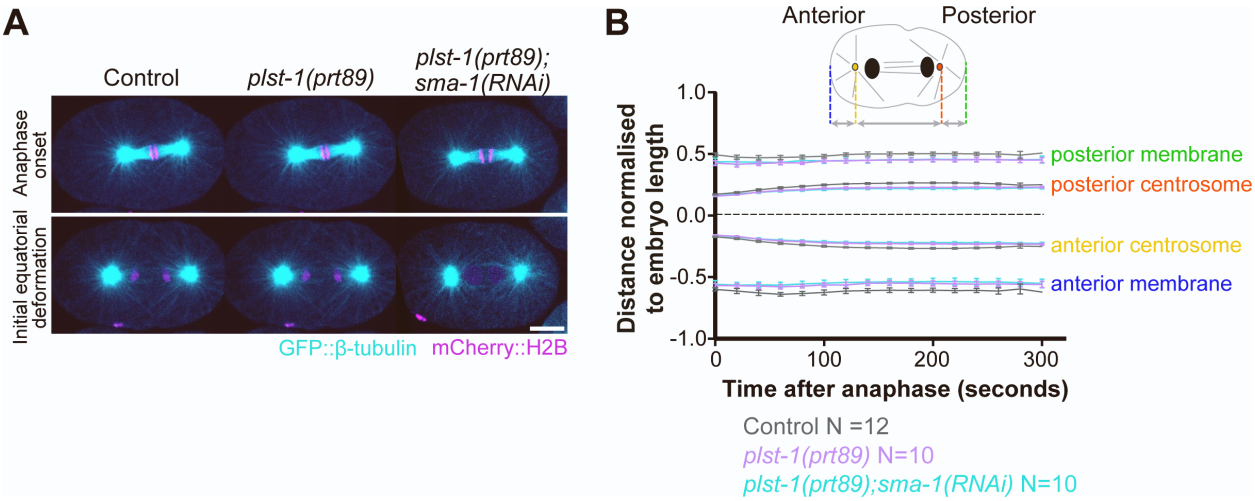

Figure S3. Mitotic spindle morphology and positioning is normal in *plst-1(prt89)* and *plst-1(prt89);sma-1(RNAi)* embryos. Related to Figure 5.

(A) Images of the central plane in one-cell embryos co-expressing GFP::β-tubulin and mCherry::histone H2B at anaphase onset and equatorial shallow deformation. Scale bar, 10 µm. **(B)** Centrosome positioning (mean ± 95% CI) along the anterior-posterior axis of the embryo over time after anaphase onset. Dashed line indicates the midpoint between the two centrosomes. N indicates the number of embryos analyzed.

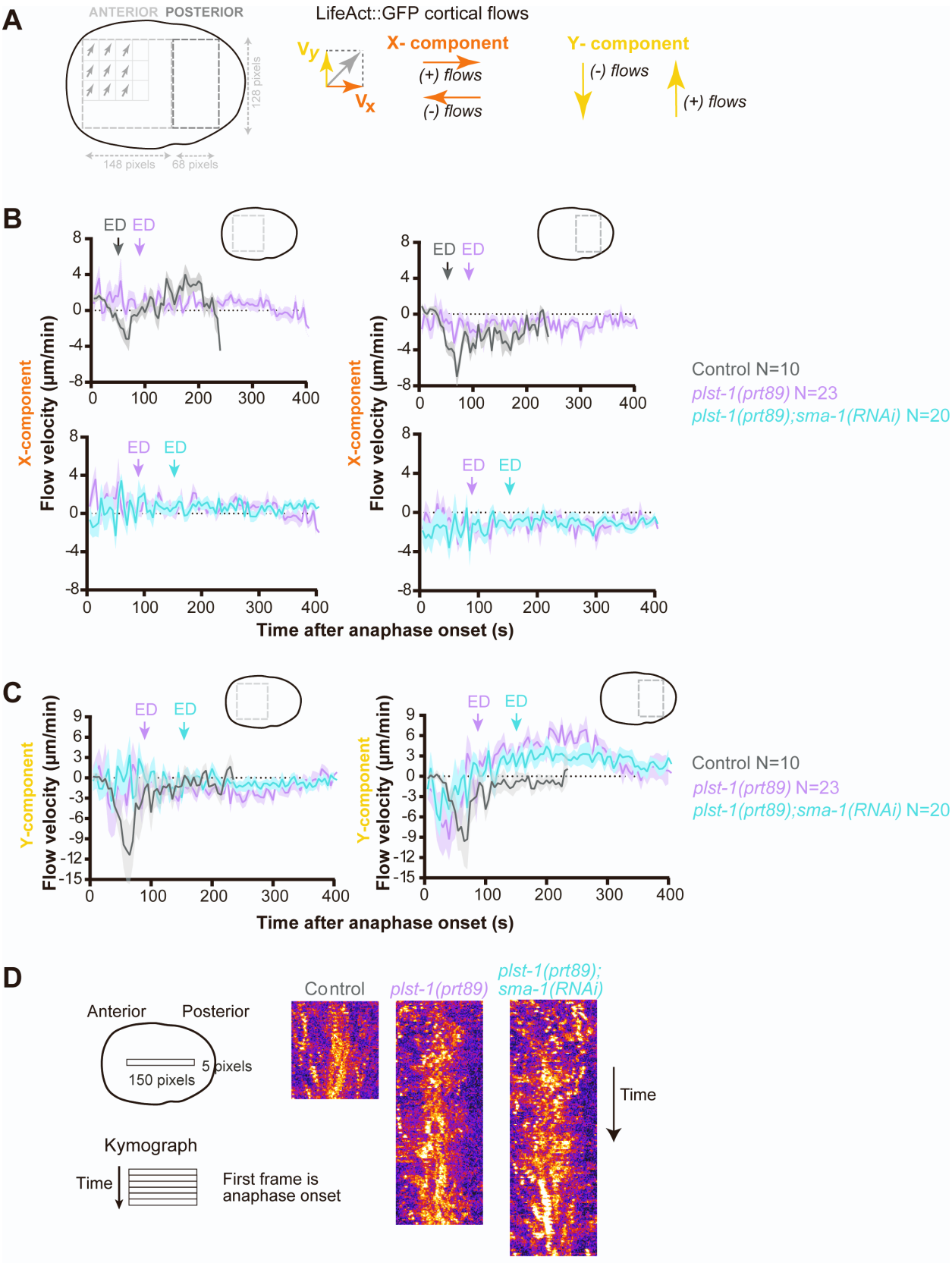
A
ANTERIOR POSTERIOR
128 pixels
148 pixels
68 pixels
LifeAct::GFP cortical flows
Vy
Vx
X- component
(+) flows
(-) flows
Y- component
(-) flows
(+) flows
B
ED ED
X-component
Flow velocity (µm/min)
Time after anaphase onset (s)
Control N=10
plst-1(prt89) N=23
plst-1(prt89);sma-1(RNAi) N=20
C
Y-component
Flow velocity (µm/min)
Time after anaphase onset (s)
Control N=10
plst-1(prt89) N=23
plst-1(prt89);sma-1(RNAi) N=20
D
Anterior
Posterior
5 pixels
150 pixels
Kymograph
Time
First frame is anaphase onset
Control
plst-1(prt89)
plst-1(prt89); sma-1(RNAi)
Time

Figure S4. Failure of cytokinesis in *plst-1(prt89);sma-1(RNAi)* embryos is not due to perturbed F-actin cortical flows. Related to Figure 5.

(A) Schematic illustrating the analysis of cortical F-actin flows by particle image velocimetry. X- and Y-components of the velocity vectors in the anterior or posterior regions of the embryo were averaged for each time point after anaphase onset. For the X-component, negative velocity values indicate posterior-anterior oriented flows and positive velocity values indicate anterior-posterior oriented flows. **(B,C)** X-component *(B)* or Y-component *(C)* flow velocities (mean ± SEM) at anterior *(left)* and posterior *(right)* cortex over time after anaphase onset in embryos expressing LifeAct::GFP. ED, initial equatorial deformation. Posterior-anterior directed flows in control embryos were particularly prominent on the posterior side, initiated before equatorial deformation, and peaked shortly thereafter (panel B, top right). F-actin cortical flows in *plst-1(prt89)* and *plst-1(prt89);sma-1(RNAi)* embryos were erratic and decreased in velocity (panel B, bottom right). N indicates the number of embryos analyzed. **(D)** Kymographs of the region indicated in the schematic on the left showing LifeAct::GFP cortical flows along the longitudinal axis in one-cell embryos, starting at anaphase onset.

A
Control
NMY-2::mCherry
LifeAct::GFP
sma-1(RNAi)
NMY-2::mCherry
LifeAct::GFP
plst-1(prt89)
NMY-2::mCherry
LifeAct::GFP
plst-1(prt89);sma-1(RNAi)
NMY-2::mCherry
LifeAct::GFP
50 s

Figure S5. Myosin coalescence into bright puncta in *plst-1(prt89);sma-1(RNAi)* embryos coincides with F-actin cluster formation. Related to Figures 5 and 6.

(A) Images of the equatorial cortical region in one-cell embryos co-expressing NMY-2::mCherry and LifeAct::GFP. First frame corresponds to the initial enrichment of NMY-2::mCherry at the cell equator. Scale bar, 10 μm.

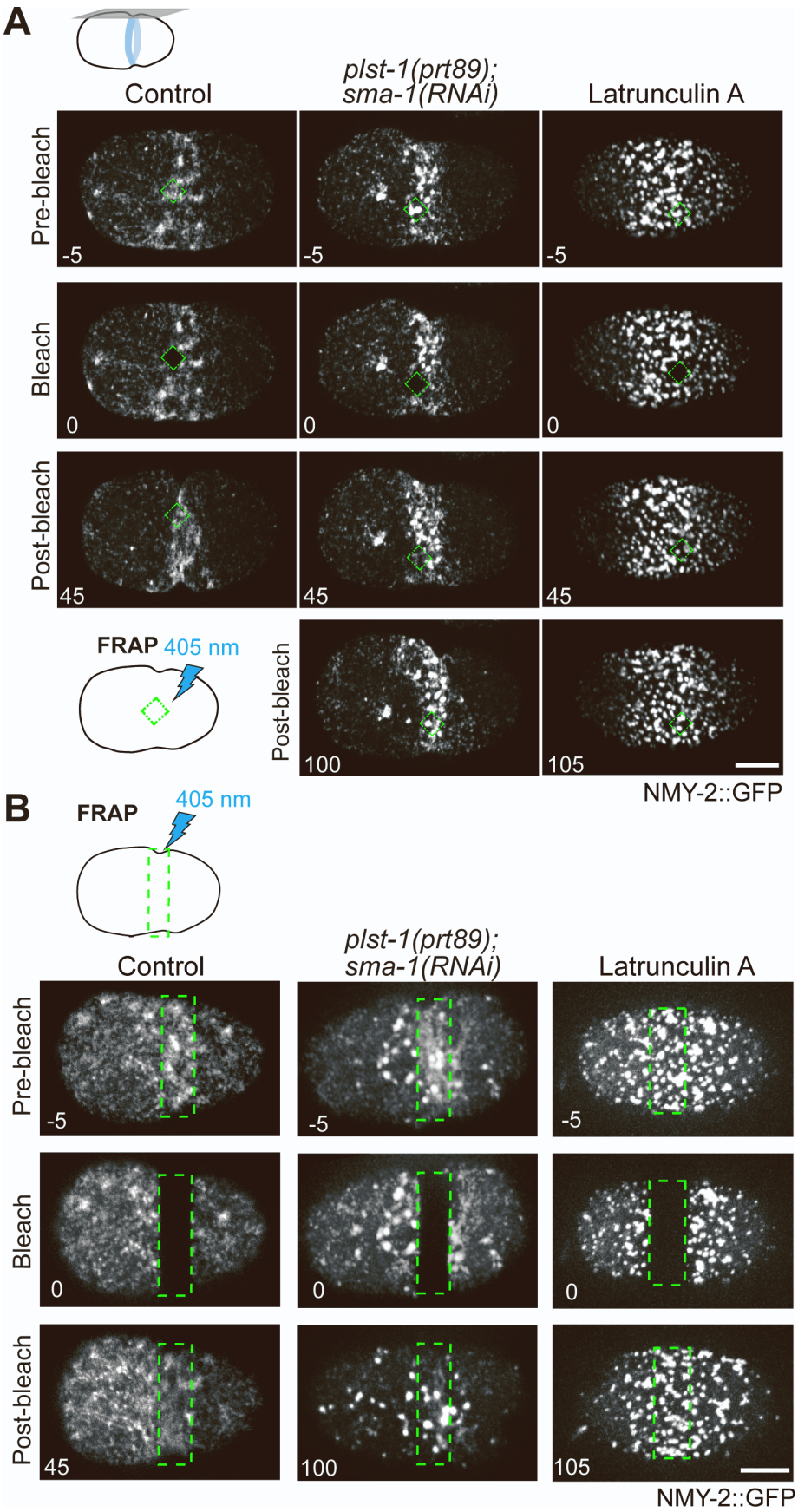
A
Control
plst-1(prt89); sma-1(RNAi)
Latrunculin A
Pre-bleach
Bleach
Post-bleach
-5
0
45
100
105
FRAP 405 nm
NMY-2::GFP
B
FRAP
405 nm
Control
plst-1(prt89); sma-1(RNAi)
Latrunculin A
Pre-bleach
Bleach
Post-bleach
-5
0
45
100
105
NMY-2::GFP

Figure S6. Fluorescence recovery after photobleaching of NMY-2::GFP at the cell equator. Related to Figure 6.

(A,B) Images of the cortex in *plst-1(prt89);sma-1(RNAi)* and Latrunculin A-treated one-cell embryos expressing NMY-2::GFP just before and after photobleaching of a portion *(A)* or the entire *(B)* cell equator at initial equatorial deformation, when myosin puncta start accumulating at the cell equator in *plst-1(prt89);sma-1(RNAi)* embryos. Numbers indicate the time in seconds relative to the photobleaching event. Schematics show the photobleached regions. Scale bars, 10 μm.

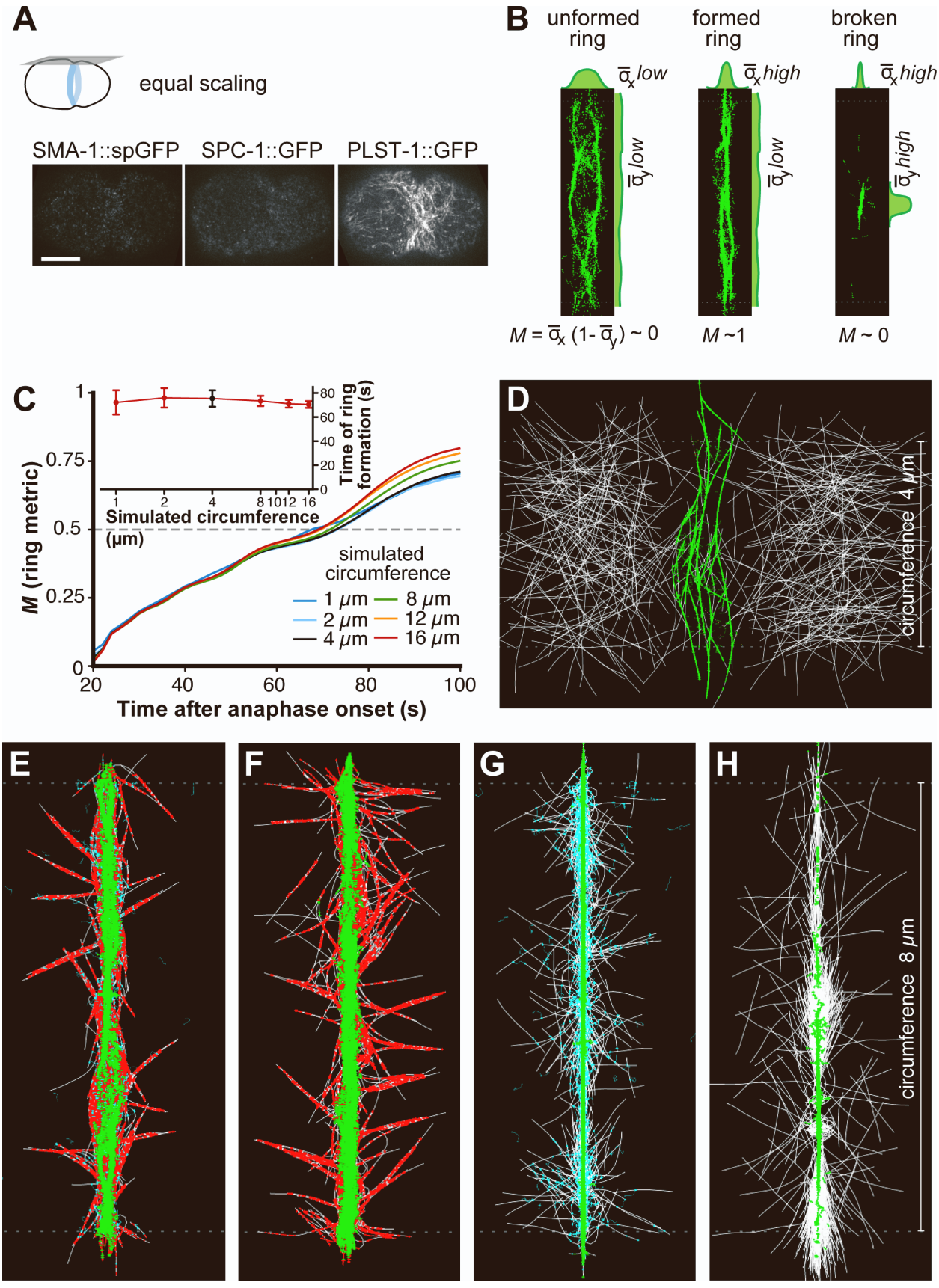
A
equal scaling
SMA-1::spGFP
SPC-1::GFP
PLST-1::GFP
B
unformed ring
formed ring
broken ring
$\bar{\sigma}_x$ low
$\bar{\sigma}_y$ low
$\bar{\sigma}_x$ high
$\bar{\sigma}_y$ low
$\bar{\sigma}_x$ high
$\bar{\sigma}_y$ high
$M = \bar{\sigma}_x (1 - \bar{\sigma}_y) \sim 0$
$M \sim 1$
$M \sim 0$
C
M (ring metric)
Time after anaphase onset (s)
Time of ring formation (s)
Simulated circumference (μm)
simulated circumference
1 μm
2 μm
4 μm
8 μm
12 μm
16 μm
D
circumference 4 μm
E
F
G
H
circumference 8 μm

Figure S7. Relative expression levels of GFP-tagged SMA-1 and PLST-1 in the early embryo, simulation metric calculation, and scaling and effects of no end-dwelling on depolymerizing ends. Related to Figures 3 and 7.

(A) Equally scaled images of the cortex in one-cell embryos expressing SMA-1::spGFP, SPC-1::GFP or PLST-1::GFP. Scale bar, 10 μm. **(B)** Simulation snapshots showing only myosin motors for simulations that (from left to right): fail to form a compact ring (double amount of plastin); successfully form a ring (reference simulation, same as last panel in Figure 7B); experience ring rupture (scenario with no plastins). Next to all snapshots are sketch plots that illustrate the measurements of x and y that are used for the ring metric (eq. 1). **(C)** Use of longer or shorter lengths of simulated circumference does not affect simulation results. Main plot: ring metric evolution for different circumference lengths. Inset: timing of ring formation or different circumference lengths ± SD. **(D)** Allowing motors to immediately fall off from depolymerizing barbed ends, instead of end-dwelling, leads to the gradual removal of F-actin from the ring midline and the ring forms with only a few F-actin fibers. **(E-H)** Simulation snapshots at 100 s after anaphase for scenarios with **(E)** all elements, **(F)** no spectrin, **(G)** no plastin, and **(H)** no plastin and no spectrin. Color legend: white - actin fibers, green - myosin, red - plastin, and cyan - βH/α-spectrin tetramer.

Fluorescent probe (expressed from transgene or endogenous locus; found in which strains)	**Method used for strain generation**	**Test of functionality**	**Reference**
LifeAct::GFP (transgene; GCP22, GCP927, GCP1163, GCP1164, GCP1169, GCP1170, GCP1176, GCP1187)	Bombardment	Normal cytokinesis timing in 1-cell embryo. Normal strain growth.	[S8]
LifeAct::RFP (transgene; GCP1207)	Bombardment	Normal cytokinesis timing in 1-cell embryo. Normal strain growth.	[S9]
PLST-1::GFP (endogenous locus; GCP831, GCP832, RZB217)	CRISPR/Cas9[a]	Normal cytokinesis timing in 1-cell embryo. Normal strain growth.	[S8]
NMY-2::GFP (endogenous locus; GCP113 and GCP570)	CRISPR/Cas9[a]	Normal cytokinesis timing in 1-cell embryo. Normal strain growth.	[S8]
NMY-2::mCherry (transgene; GCP22, GCP927, GCP1163, GCP1164, GCP1169, GCP1170, GCP1176, GCP1187)	MosSci[b], Chromosome II	NMY-2::mCherry is able to replace endogenous nmy-2. Normal strain growth.	[S10]
GFP::ANI-1 (transgene; OD130)	Bombardment	Normal strain growth. Pattern of localization of GFP::ANI-1 identical to that observed in strain MDX29, where the endogenous locus of ani-1 is tagged with mNeonGreen (Rehain-Bell et al., 2017).	[S11]
UNC-59::GFP (transgene; OD121)	Bombardment	UNC-59::GFP expression under the control of the pie-1 regulatory sequences	[S12]

		rescues the localization of UNC-61 (the other septin with which UNC-59 oligomerizes)	
SMA-1::splitGFP (endogenous locus; GCP991, GCP1207, GCP1208)	CRISPR/Cas9[a]	Normal strain growth.	This study
SPC-1::GFP (endogenous locus; GOU2936)	CRISPR/Cas9 [a]	Normal strain growth.	[S13]

[a] CRISPR/Cas9 - Clustered Regularly Interspaced Short Palindromic Repeats/CRISPR-associated protein 9

[b] MosSci - Mos1-mediated Single Copy Insertion

Table S1. Summary of fluorescent tagged proteins used in this study. Related to Figures 1-7.

Oligonucleotide purpose	**Oligonucleotide sequence (5'-3')**
For production of dsRNA against ani-1 (Y49E10.19)_Fwd	taatacgactcactataggTCAAACTCAATGGAGAGGACAA-3' *T7 promoter sequence is in lowercase*
For production of dsRNA against ani-1 (Y49E10.19)_Rev	aattaaccctcactaaaggCATTGTGCTTCAAATTCCTCAC *T3 promoter sequence is in lowercase*
For production of dsRNA against atn-1 (W04D2.1)_Fwd	aattaaccctcactaaaggCAAAAGCTCGAGGACTACCG *T3 promoter sequence is in lowercase*
For production of dsRNA against atn-1 (W04D2.1)_Rev	taatacgactcactataggAGCTGCGAATCTCTTCTTGG *T7 promoter sequence is in lowercase*
For production of dsRNA against fln-1 #1 (Y66H1B.2)_Fwd	aattaaccctcactaaaggCCGATTTCCAACTTCACTTCC *T3 promoter sequence is in lowercase*
For production of dsRNA against fln-1 #1 (Y66H1B.2)_Rev	taatacgactcactataggGACTTCACCAGCAACCTTAAC *T7 promoter sequence is in lowercase*
For production of dsRNA against fln-1 #2 (Y66H1B.2)_Fwd	aattaaccctcactaaaggTGGATGGGCAACTGTTTATG *T3 promoter sequence is in lowercase*
For production of dsRNA against fln-1 #2 (Y66H1B.2)_Rev	taatacgactcactataggGAGCTCCTCCTTCAGAGAAT *T7 promoter sequence is in lowercase*
For production of dsRNA against plst-1 (Y104H12BR.1)_Fwd	aattaaccctcactaaaggACTCGGAGTCCATGGAAATG *T3 promoter sequence is in lowercase*
For production of dsRNA against plst-1 (Y104H12BR.1)_Rev	taatacgactcactataggCACCATTTTTGGCTTCACCT *T7 promoter sequence is in lowercase*
For production of dsRNA against unc-59 (W09C5.2)_Fwd	taatacgactcactataggCGTGAAACTCGTGGAGAACA *T7 promoter sequence is in lowercase*
For production of dsRNA against unc-59 (W09C5.2)_Rev	aattaaccctcactaaaggTTGTGGTGGAGTTCAACGTG *T3 promoter sequence is in lowercase*
For production of dsRNA against unc-61 (Y50E8A.4)_Fwd	taatacgactcactataggAGCTGTCGAAGCTGGATTTC *T7 promoter sequence is in lowercase*
For production of dsRNA against unc-61 (Y50E8A.4)_Rev	aattaaccctcactaaaggACGGCTGAACTCGTCTTGAT *T3 promoter sequence is in lowercase*
For production of dsRNA against unc-70 (K11C4.3)_Fwd	aattaaccctcactaaaggCACTGTCTTGAGAACGTTGAG *T3 promoter sequence is in lowercase*

For production of dsRNA against unc-70 (K11C4.3)_Rev	taatacgactcactataggAATGGATTTCTCATCAGGTTGG *T7 promoter sequence is in lowercase*
For production of dsRNA against erm-1 (C01G8.5)_Fwd	aattaaccctcactaaaggCTTCTACGCTCCACGACTCC *T3 promoter sequence is in lowercase*
For production of dsRNA against erm-1 (C01G8.5)_Rev	taatacgactcactataggCTCCATATGCAGAACGTCGTA *T7 promoter sequence is in lowercase*
Single guide RNA #1 used to generate *sma-1*ΔABD#1 mutant	TCACGCATTCGGACACTGC
Single guide RNA #2 used to generate *sma-1*ΔABD#1 mutant	GTGCAACTCCTTTCTTAAT
Single guide RNA #3 used to generate *sma-1*ΔABD#1 mutant	ATTGACTTCTCGTCAGGCC
Repair template used to generate *sma-1*ΔABD#1 mutant	cagGTTCGTGTTCCAACAAGTGGTGCACCACCAGTTCG CGCAGATGCCAATGGAACAGATCA**G**GACGAGTTCAA TAATGAGACACTGTACTTTGAAAGATCACGCATTCGG ACACTGCA**A**GACGAACGTGTGAAGCAAAAGACTGAG ATGACAGGAGCTCGACGTATTGCTAATgtaagtgtttataagtt catg *in bold are silent mutations introduced to avoid repair template recognition by Cas9 or to maintain codon balance; bases in lowercase indicate intron regions*
For screening of *sma-1*ΔABD#1 successful events_Fwd	GGAAAGACGCTGAGCTAGTA
For screening of *sma-1*ΔABD#1 successful events_Rev	CTCCTTGTACTTTGGTGGTTTC
crRNA #1 used to generate *sma-1*ΔABD#2 mutant	CTCGTCTTGATCTGTTCCAT
crRNA #2 used to generate *sma-1*ΔABD#2 mutant	TTAAATTTTTCAGGATGAGG
Repair template used to generate *sma-1*ΔABD#2 mutant	aaagttttaaagatccgaaaaaaaactgagaacgtttagaaatatttaacagttcaattagc atcaagttcataatgatttttttcagGTTCGTGTTCCAACAAGTGGTGC ACCACCAGTTAATCGG-intron3/4- GATGAGGAAGAGCGTGGAGAGCGAAAACATGCCAA AGATGCCTTGCTGTTGTGGTGTCAGAGAAAAACAGC TGGATATCCAAATGTTCGCATCGAGAACTTCACTACA AGTTGG *bases in lowercase indicate intron regions; intron3/4 as in sma-1 transcript R31.1a, Wormbase version WS279*
For screening of *sma-1*ΔABD#2 successful events_Fwd	AACGGAAAGACGCTGAGCTAGT

For screening of *sma-1*ΔABD#2 successful events_Rev	GATCCGGACGGTGCGAATGG
crRNA #1 used to generate *sma-1*ΔSH3 mutant	ATTGACTGGTAGTAGCAGTG
crRNA #2 used to generate *sma-1*ΔSH3 mutant	TCTAGACTGACCATGACCTT
Repair template used to generate *sma-1*ΔSH3 mutant	gcagGAGTGACATCAGTCGACTCGAGGAGATGCAAAG TCAGCTAGCAAACGAAGGTCATGGTCAGTCTAGAAA AATCGAAGTTCGTCAACATAAGATCAA *bases in lowercase indicate intron regions*
For screening of *sma-1*ΔSH3 successful events_Fwd	CAGTCGACTCGAGGAGATGC
For screening of *sma-1*ΔSH3 successful events_Rev	TGGTTTCAAATCACGCTCCA
Single guide RNA #1 used to generate *sma-1*ΔPH mutant	TGGGTGCTATTGACATGAA
Single guide RNA #2 used to generate *sma-1*ΔPH mutant	ACGACTTGAGCTGATTACT
Repair template used to generate *sma-1*ΔPH mutant	CGTTCAATACTCGTCGTACTCAATCAATCCGCAAAGG AAGTCGCTGGGAAGATATGGGTCCA**TCCAA**TCA**ACT GAAATC**GTATGCGTACAACGgttagttaattactatttaaattattaacc agtttgcttctcag *in bold are silent mutations introduced to avoid repair template recognition by Cas9 or to maintain codon balance*
For screening of *sma-1*ΔPH successful events_Fwd	GCAAAGACTACCGCTGATTT
For screening of *sma-1*ΔPH successful events_Rev	GTTGATCTGGACTTTGGAAGAG
Single guide RNA #1 used to generate *sma-1*Δ11SR mutant	CGTGACCTCGGTCGAGATGT
Single guide RNA #2 used to generate *sma-1*Δ11SR mutant	TTACAAGATAAGGAAGCGAC
Repair template used to generate *sma-1*Δ11SR mutant	GTGACGTTGACGAGTTTGAGCAATGGATGGCAGACA AAATGGCCAACATGGTAGCAATGGAACAGGAAGATC TTTCGAGAGCTGATCTTGCTTCCGTGAA
For screening of *sma-1*Δ11SR successful events_Fwd	AGCAGGAAGCACTCAGAACC
For screening of *sma-1*Δ11SR successful events_Rev	GCCGAGTATCTGGGAACGAG

Single guide RNA #1 used to generate *atn-1*ΔABD mutant	AGGACTGTTAGATCCAGCA
Single guide RNA #2 used to generate *atn-1*ΔABD mutant	GGACTGTTAGATCCAGCAT
Single guide RNA #3 used to generate *atn-1*ΔABD mutant	ATGCTGGATCTAACAGTCC
Repair template used to generate *atn-1*ΔABD mutant	CATACCATCAGCCGGGCTACGACTACACTCAACAAG AGGAAGAATGGGACCGTGAAGGA**TTACTG**GATCC**T** GC**C**TGGGAGGCATT**T**CGTAACATGCGTGATCCTCCAC CACCAGTTATTCGCCAACCACCACCACAGCGTGTTGT TGTTGCTCCACCTCCAGAG *in bold are silent mutations introduced to avoid repair template recognition by Cas9 or to maintain codon balance*
For screening of *atn-1*ΔABD successful events_Fwd	CCTTCTTCACACCGTTCATC
For screening of *atn-1*ΔABD successful events_Rev	GAGACAAGGACAATGGACATTTA
Single guide RNA #1 used to generate *sma-1::spGFP*	TCGGATCGTTATTCAAGCG
Single guide RNA #2 used to generate *sma-1::spGFP*	GGTATCTACTTTGAATGTT
Single guide RNA #3 used to generate *sma-1::spGFP*	TGAAGATCAGCGTGTGGTG
For screening of *sma-1::spGFP* successful events_Fwd	GCGAATTCATTACTTGGGTAGA
For screening of *sma-1::spGFP* successful events_Rev	GTCTTCCAGCTTTGGTGATAG
Single guide RNA used to generate *plst-1::mCherry*	CCATTAATCATCGGAACAAT
For screening of *plst-1::mCherry* successful events_Fwd	GGTGGCATGGATGAATTG
For screening of *plst-1::mCherry* successful events_Rev	CCAAATTTAGGCTAGAAACTCGAT

Table S2. List of oligonucleotides used in this study. Related to Figures 1-4 and 7.

Parameter	Symbol	Value Range (standard value)
Actin Rigidity	μ_{actin}	0.075 pN μm^2 [S14]
Actin Segmentation Length	l_{actin}	0.1 μm
Actin Fiber Length (initial)	L_{actin}	1 μm [S15]
Growing Speed of Barbed End	v_{b+}	0 - 0.8 μm/s (0.08 μm/s) [S16]
Shrinking Speed of Barbed End	v_{b-}	0 - 0.56 μm/s (0.056 μm/s) [S16]
Growing Speed of Pointed End	v_{p+}	0 μm/s
Shrinking Speed of Pointed End	v_{p-}	0 - 0.14, μm/s (.014 μm/s) [S16]
Switch Rate to Depolymerization	r_c	8 Hz
Switch Rate to Polymerization	r_r	4 Hz
Backbone Length of Myosin	L_{motor}	0.15 μm [S17]
Number of Binding Heads of Myosin	n	8
Binding Range of Motor Head	d_{bind}	0.01 μm
Binding Rate of Motor Head	b_{motor}	10 Hz [S18]
Unbinding Rate of Motor Head	u_{motor}	0.3 Hz [S18]
Maximum Motor Speed	v_0	0.1 μm/s [S19]
Stall Force	f_0	4 pN [S20]
Backbone Resting Length of Plastin	$l_{plastin}$	0.012 μm [S21]
Spring Stiffness	k	250 pN/μm
Binding Range of Plastin	d_{bind}	0.01 μm
Binding Rate of Plastin	$b_{plastin}$	10 Hz
Unbinding Rate of Plastin	$u_{plastin}$	0.5 Hz
Maximum Allowed Angular Difference	$\Delta\theta_{max}$	10 degrees
Rescue Probability of Plastin	$r_{plastin}$	0.1

βH-Spectrin Rigidity	$\mu_{spectrin}$	$7.5*10^{-5}$ pN μm^2 [S22]
βH-Spectrin Segmentation Length	$l_{spectrin}$	0.05 μm
βH-Spectrin Backbone Length	$L_{spectrin}$	0.15-0.35 μm (0.2 μm)
Binding Range of Binding Head	d_{bind}	0.01 μm
Binding Rate of Binding Head	$b_{spectrin}$	10 Hz
Unbinding Rate of Binding Head	$u_{spectrin}$	0.5 Hz
Rescue Probability of βH-Spectrin	$r_{spectrin}$	0.1
Width (Non Periodic Boundary)	x_0	10 μm
Height (Periodic Boundary)	y_0	1-16 μm (4 μm)
Initial Component Horizontal Range	x_i	3 μm
Background Viscosity	ν	1 pN s / μm^2 [S23]
Background Temperature	kT	0.0042 pN μm
Fiber Count	N_F	94-1,500 (375)
Motor Count	N_M	260-4,168 (1,042)
Plastin Count	N_P	0-120,000 (30,000)
βH-spectrin Count	N_S	0-5,600 (1,400)

Table S3. Cytosim parameters used in simulations (where parameters were varied, base values are shown in parentheses). Related to Figures 7 and S7.

Supplemental References

S1. Moorthy, S., Chen, L., and Bennett, V. (2000). Caenorhabditis elegans beta-G spectrin is dispensable for establishment of epithelial polarity, but essential for muscular and neuronal function. J. Cell Biol. *149*, 915–930.

S2. Chan, F.-Y., Silva, A.M., Saramago, J., Pereira-Sousa, J., Brighton, H.E., Pereira, M., Oegema, K., Gassmann, R., and Carvalho, A.X. (2019). The ARP2/3 complex prevents excessive formin activity during cytokinesis. Mol. Biol. Cell *30*, 96–107.

S3. Kovacevic, I., and Cram, E.J. (2010). FLN-1/filamin is required for maintenance of actin and exit of fertilized oocytes from the spermatheca in C. elegans. Dev. Biol. *347*, 247–257.

S4. Maddox, A.S., Habermann, B., Desai, A., and Oegema, K. (2005). Distinct roles for two C. elegans anillins in the gonad and early embryo. Development *132*, 2837–2848.

S5. Moulder, G.L., Cremona, G.H., Duerr, J., Stirman, J.N., Fields, S.D., Martin, W., Qadota, H., Benian, G.M., Lu, H., and Barstead, R.J. (2010). α-actinin is required for the proper assembly of Z-disk/focal-adhesion-like structures and for efficient locomotion in Caenorhabditis elegans. J. Mol. Biol. *403*, 516–528.

S6. Ono, S. (2001). The Caenorhabditis elegans unc-78 gene encodes a homologue of actin-interacting protein 1 required for organized assembly of muscle actin filaments. J. Cell Biol. *152*, 1313–1319.

S7. Maddox, A.S., Lewellyn, L., Desai, A., and Oegema, K. (2007). Anillin and the septins promote asymmetric ingression of the cytokinetic furrow. Dev. Cell *12*, 827–835.

S8. Leite, J., Chan, F.-Y., Osório, D.S., Saramago, J., Sobral, A.F., Silva, A.M., Gassmann, R., and Carvalho, A.X. (2020). Equatorial Non-muscle Myosin II and Plastin Cooperate to Align and Compact F-actin Bundles in the Cytokinetic Ring. Front Cell Dev Biol *8*, 573393.

S9. Ding, W.Y., Ong, H.T., Hara, Y., Wongsantichon, J., Toyama, Y., Robinson, R.C., Nédélec, F., and Zaidel-Bar, R. (2017). Plastin increases cortical connectivity to facilitate robust polarization and timely cytokinesis. J. Cell Biol. *216*, 1371–1386.

S10. Osório, D.S., Chan, F.-Y., Saramago, J., Leite, J., Silva, A.M., Sobral, A.F., Gassmann, R., and Carvalho, A.X. (2019). Crosslinking activity of non-muscle myosin II is not sufficient for embryonic cytokinesis in C. elegans. Development *146*.

S11. Lewellyn, L., Carvalho, A., Desai, A., Maddox, A.S., and Oegema, K. (2011). The chromosomal passenger complex and centralspindlin independently contribute to contractile ring assembly. J. Cell Biol. *193*, 155–169.

S12. Carvalho, A., Desai, A., and Oegema, K. (2009). Structural memory in the contractile ring makes the duration of cytokinesis independent of cell size. Cell *137*, 926–937.

S13. Jia, R., Li, D., Li, M., Chai, Y., Liu, Y., Xie, Z., Shao, W., Xie, C., Li, L., Huang, X., et al. (2019). Spectrin-based membrane skeleton supports ciliogenesis. PLoS Biol. *17*, e3000369.

S14. Gittes, F., Mickey, B., Nettleton, J., and Howard, J. (1993). Flexural rigidity of microtubules and actin filaments measured from thermal fluctuations in shape. J. Cell Biol. *120*, 923–934.

S15. Burlacu, S., Janmey, P.A., and Borejdo, J. (1992). Distribution of actin filament lengths measured by fluorescence microscopy. American Journal of Physiology-Cell Physiology *262*, C569–C577.

S16. Shekhar, S., and Carlier, M.-F. (2017). Enhanced depolymerization of actin filaments by ADF/Cofilin and monomer funneling by capping protein cooperate to accelerate barbed-end growth. Curr. Biol. *27*, 1990–1998.e5.

S17. Billington, N., Wang, A., Mao, J., Adelstein, R.S., and Sellers, J.R. (2013). Characterization of three full-length human nonmuscle myosin II paralogs. J. Biol. Chem. *288*, 33398–33410.

S18. Guo, B., and Guilford, W.H. (2006). Mechanics of actomyosin bonds in different nucleotide states are tuned to muscle contraction. Proc. Natl. Acad. Sci. U. S. A. *103*, 9844–9849.

S19. Barua, B., Nagy, A., Sellers, J.R., and Hitchcock-DeGregori, S.E. (2014). Regulation of nonmuscle myosin II by tropomyosin. Biochemistry *53*, 4015–4024.

S20. Walcott, S., Warshaw, D.M., and Debold, E.P. (2012). Mechanical coupling between myosin molecules causes differences between ensemble and single-molecule measurements. Biophys. J. *103*, 501–510.

S21. Matsudaira, P., Mandelkow, E., Renner, W., Hesterberg, L.K., and Weber, K. (1983). Role of fimbrin and villin in determining the interfilament distances of actin bundles. Nature *301*, 209–214.

S22. Stokke, B.T., Mikkelsen, A., and Elgsaeter, A. (1985). Human erythrocyte spectrin dimer intrinsic viscosity: temperature dependence and implications for the molecular basis of the erythrocyte membrane free energy. Biochim. Biophys. Acta *816*, 102–110.

S23. Daniels, B.R., Masi, B.C., and Wirtz, D. (2006). Probing single-cell micromechanics in vivo: the microrheology of C. elegans developing embryos. Biophys. J. *90*, 4712–4719.